Thermo-mechanical simulation of Si processing for photovoltaic applications

by

Ambrish Chandra Sinha

B.Tech., Indian Institute of Technology Kanpur India, 2011

A THESIS SUBMITTED IN PARTIAL FULFILLMENT OF
THE REQUIREMENTS FOR THE DEGREE OF

MASTER OF APPLIED SCIENCE

in

THE COLLEGE OF GRADUATE STUDIES

(Mechanical Engineering)

THE UNIVERSITY OF BRITISH COLUMBIA

(Okanagan)

May 2017

Committee

The undersigned certify that they have read, and recommend to the College of Graduate Studies for acceptance, a thesis entitled: Thermo-mechanical simulation of Si processing for photovoltaic applications submitted by Ambrish Chandra Sinha in partial fulfilment of the requirements of the degree of Master of Applied Science

Dr. Andre Phillion, Materials Engineering, McMaster University

Supervisor, Professor (please print name and faculty/school above the line)

Dr. Steve Cockroft, Materials Engineering, UBC Vancouver

Co-Supervisor, Professor (please print name and faculty/school above the line)

Dr. Daan Maijer, Materials Engineering, UBC Vancouver

Co-Supervisor, Professor (please print name and faculty/school above the line)

Dr Stephen O'Leary, Applied Science/School of Engineering

University Examiner, Professor (please print name and faculty/school above the line)

5/24/2017

(Date Submitted to Grad Studies)

Abstract

Wafers for solar cell applications are increasingly being produced via wire sawing of directional solidified multi-crystalline silicon (mc-Si) ingots. During these two processes, defects such as dislocations arise in the material which reduce the final electrical efficiency of the solar cells. Furthermore, processing conditions during these processes can also influence the surface unevenness and warpage in the final wafers. Previously, several researchers have developed finite element models of mc-Si directional solidification process to understand the growth of residual stress and dislocation in the ingots under different cooling conditions, boundary conditions and geometry. Researchers have also developed analytical and finite element models to understand the temperature variation and the material removal behaviour during wire sawing process. However, there has not been much work done in understanding the influence of pre-existing residual stress in the work piece (directionally cooled mc-Si ingots) on the wafer quality during wire sawing.To investigate this, in this work, thermal-stress finite element models were developed for directional solidification and wire sawing process, with later taking the results from former as the stress/strain and dislocation initial conditions. Dislocation creep behaviour of Si was used as the material constitutive behaviour in both the models. The input parameters for the casting model were 3 different cooling rates. The wire sawing simulation was done in the top, middle and bottom section of these ingots. The warpage was, therefore, studied in 9 wafers. These models also simulated the spacial/temporal variation of in-elastic deformation and dislocation density in the ingot and the wafers. The predicted results from the casting model were in good agreement with the past models. The predicted warpage from the wire sawing simulation, however, was less compared to the warpage observed

in the industry. This variation in the results may be due to the several assumptions and simplifications taken in the model in-terms of the constitutive behaviour, material properties and boundary conditions.

Preface

The work outlined in this thesis was carried out in UBC's Okanagan Solidification Processing and Simulation Lab by Ambrish Chandra Sinha under the guidance of Dr. Andre Phillion. The work was done for Toronto based PRISED Solar and it involved discussions with PRISED Solar's founder Dr. Wahid Shams-Kolahi. Ambrish Chandra Sinha was responsible for designing and developing the simulatiosn and Dr. Andre Phillion helped in interpreting the results.

Portions of Chapter 2, 4 and 5 have been presented at a conference:
A. Sinha and A. Phillion, "Modelling of warpage in silicon wafer during wiresawing," in *28th Canadian Material Science Conference*, Hamilton, Canada, 2016

Table of Contents

List of Tables

List of Figures

List of Acronyms

Metallurgical grade Si - MGS

Electronic grade Si - EGS

Solar grade Si - SGS

Multi-crystalline Si - mc-Si

Ductile to brittle transition temperature - DBTT

Haasen Alexander Sumino model - HAS model

Finite element - FE

Directional solidification - DS

List of Symbols

Strain - ϵ

Elastic strain - ϵ_{el}

Inelastic strain - ϵ_{ie}

Plastic strain - ϵ_{p}

Creep strain - ϵ_{creep}

Stress - σ

Effective stress - σ_{eff}

Upper yield stress - σ_{ys}^{u}

Lower yield stress - σ_{ys}^{l}

Material stiffness - D

Temperature - T

Melting temperature - Tm

Dislocation density - N_m

Dislocation velocity - v

Boltzman's constant - k_B

Hardening coefficient - D

Activation coefficient - Q

Constant pressure specific heat - c_p

Thermal conductivity - k

Thermal expansion coefficient - α'

Effective thermal expansion coefficient - α

Youngs modulus - E

Poissons ration - ν

Acknowledgements

I would like to thank my supervisor, Dr. André Phillion, who provided me this great opportunity to work under him and among a very hard working and talented peer lab group. I deeply appreciate his valuable mentorship in this journey towards becoming a researcher, an engineer and a problem solver. I thank him for pushing me towards becoming a high work ethics individual with great writing and presentation skills.

I would also like to sincerely thank Dr. Steve Cockcroft and Dr. Daan Maijer for their guidance and agreeing to be on my supervising committee. I would also like to thank Dr. Carl Reily for the occasional cluster related help.

I would like to acknowledge the Natural Sciences and Engineering Research Council of Canada for funding my research and studies at UBC-Okanagan. I also thank PRISED Solar, Toronto and Dr Wahid Shams-Kolah for offering this project.

I am grateful to the many amazing teachers, professors here at UBCO, especially Dr. Bichler and Dr. Milani and at IIT Kanpur, especially Dr. Mondal for imparting their knowledge which enabled me to finish this challenging task.

I am also grateful for the support of my labmates, especially Saibal for helping me with the doubts I had with Abaqus. I would also like to thank Amit, for our many intellectual discussions during coffee and lunch breaks. I would also like to thank my friends in Kelowna, especially Vishank, Parul, and William, and my friends in India for their support and many encouragements. I would like to thank my dear landlord, David Thompson, for offering me not just a house, but also a home.

Lastly, I would like to say that I will always be in-debt to my mother, father and brother, for their constant love and support during my masters, and before that.

Dedication

To my parents, who have constantly motivated me to never give up.

Chapter 1

Introduction

Increase in population and our standards of living has led to an increase in demand for basic human needs such as food and energy, putting significant pressure on sectors such as agriculture, energy production etc. The International Energy Outlook has forecast a 48% rise in global energy consumption between 2012 and 2040 [39]. The unprecedented levels of fossil fuels required to be burnt for this much energy production is simply alarming for two reasons, First the catastrophic environmental impacts, and second fossil fuels are a finite resource. So the world urgently requires stable and consistent clean energy technology.

Solar energy is a clean alternative to fossil fuel, that has received considerable academic, political and industrial interest in recent years. Harnessing energy through the use of solar panels is one of the most affordable clean energy technologies that has been developed. However, the electricity per unit cost from solar power is still quite high as compared to conventional sources making it unaffordable for wide-spread use. Thus, further research is required to develop cheaper technologies that are able to create efficient yet durable solar cells.

1.1 Materials requirements for photovoltaic application

Although solar cell could have several meaning such as photothermal solar cell, photovoltaic solar cells etc, in this work, solar cells are mentioned in context of photovoltaic solar cell only. A photovoltaic solar cell is an electrical device that converts

light energy into electrical energy via the photovoltaic effect in which electron flow is generated by absorbing photons. Solar cells are produced from thin slices or wafers of a suitable material.

In order to be a good solar cell, the wafer material is required to have good efficiency in terms of the quantity of electricity produced from a given amount of light. Among many factors, this efficiency is also dependent on the defects present inside the material such as dislocations, grain boundary and impurity atoms to name a few. Crystalline materials being defect-free have a good efficiency, and thus fit the description for a photovoltaic material, but are very costly to produce. Apart from the efficiency, the material should also have good mechanical strength in order to withstand the wafer development process and final deployment in external environments. To save costs, wafers are produced at a thickness of 300-500 microns. At such thicknesses, the chance of breaking via brittle fracture increases significantly. The mechanical properties of the material also influence surface crack formation during the sawing process, which affects the final strength of the wafers [30]. A material with good mechanical properties is therefore imperative for the production of durable solar cells.

1.2 Si as a photovoltaic material

Si is widely used to make solar cell wafers. It is used, among other semiconductors, because being a widely used electronic material, its physical and chemical properties have already been well-studied. Technologies, such as the Czochralski and Float-zone processes, already exist to produce single crystal Si (c-Si) at the industrial scale. It should be noted that there are materials, such as CdTe (1.49 eV) and GaAs (1.43 eV), with band gap closer to the visible spectrum (1.5 eV), but Si (1.1 eV) is used over them because it is more economical to produce it industrially [48].

Si for electronic and solar applications is obtained through a series of extraction and purification steps, the first of which is extraction from silica. The Si extracted

from silica is 98% pure, and is referred to as metallurgical grade Si (MGS) [48]. This is used for many different applications, most notably as an alloying element in aluminum alloy products. Si used for electronic applications, referred to as electronic grade Si (EGS), requires an additional purity, up to 99.9999999% (also known as Nine nines or 9N pure) [48]. The purification of MGS into EGS is accomplished via chemical purification. EGS is then used as feedstock material in the Czochralski method to obtain single crystal Si which is used in electronic industry. Initially, single crystalline EGS was also used for solar cell wafer fabrication. However, since single crystalline EGS is expensive, solar panels made out of it are expensive too. This expense is not justified, since Si used for solar cells, called solar grade Si (SGS), requires only 5N (99.999%) purity levels [48].

In recent years, research on producing SGS has focused on directional solidification with MGS as feedstock material. However, directional solidification produces multi-crystalline Si (mc-Si) ingots instead of c-Si ingots, which are less efficient due to the presence of grain boundaries [12]. Apart from that, mc-Si ingots are usually contaminated with impurities such as O, Fe, Cr, Ni, Ti and Cu which further lead to efficiency loss [8, 9]. These impurities are incorporated from the crucible during the directional solidification process [18] or can be already present in the MGS feedstock. So a cost saving in producing ingots through directional solidification comes at an efficiency loss in the solar cells. However, this loss in efficiency can be reduced by efficiently changing the process parameters used during directional solidification to both improve purity and reduce grain boundary.

Several companies are trying to develop even more efficient method of developing SGS. The industrial partner for this study, PRISED solar, a company based in Toronto, Canada, has developed a purifying method to upgrade MGS into SGS. This technique involves migration of impurities to internal surfaces using microwave technology and then trapping them at neutral sites using gettering agents [38]. This purification is done on a wafer or pellet geometry. These wafers can be made from wire sawing of MGS ingots made via directional solidification process.

1.3 Directional solidification

The directional solidification process is a casting technique in which the heat is taken out of the melt uni-directionally. The directional heat flux extraction facilitates formation of columnar grain structure. This process also facilitates reduction in grain boundaries. Most of the mc-Si for solar cells are produced using directional solidification.

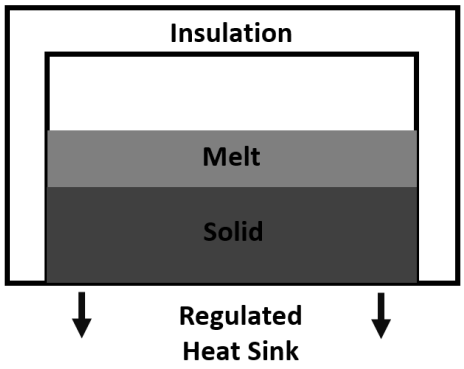

Figure 1.1: Directional Solidification

As shown in Figure 1.1, MGS is provided as feedstock for the directional solidification process and is converted into molten Si. Heat is then extracted from the bottom surface only, while the other surfaces are insulated to ensure a (nearly) planer solidification front. This process has an additional advantage in that it can be used to purify the feedstock through a process known as zone refining, or component segregation. Segregation is the physical phenomenon whereby a constituent is rejected from the solid phase into the melt due to the fact that the composition exceeds the solid solubility limits. The amount of segregation is measured by the segregation coefficient k_0 given as,

$$k_0 = \frac{C_S}{C_L}$$

where C_S and C_L are the constituents' concentration in the solid and liquid phases, respectively. For most constituents dissolved in Si, $k_0 < 1$ [45] which means the impurity prefers to stay in the liquid. As solidification within an ingot reaches completion,

the impurities concentrate at the top, as it is the last part to solidify. This process can be repeated several times to further segregate and remove impurities. Specifically, after multiple directional solidification loops, the top part containing impurities can be cut off and scrapped.

The rate of cooling is a crucial factor of directional solidification. A slow cooling rate leads to large grain sizes with less grain boundary area and less residual stress, and thus is preferred over a faster cooling. But a slow cooling rate also leads to an increase in manufacturing time and cost. A higher rate of cooling reduces manufacturing time but leads to a higher level of dislocation density and residual stress within the mc-Si ingot [31, 37]. Higher levels of dislocation density reduce the efficiency of solar cells [12, 17]. The rate of cooling, therefore, should be optimised in order to ensure both the profitability and the performance of mc-Si ingots.

1.4 Wafer production by Wire sawing

SGS ingots from the directional solidification process are converted into solar wafers via sawing techniques. Among the many sawing techniques, multi wire sawing is the most efficient since it can be used to cut all of the ingot at once. 80% of the wafers for solar cells are produced industrially via multi wire sawing [30]. During this process, SGS ingots are glued to a substrate holder and placed in a wire saw which then slices them into thin wafers. This process is shown via the schematic in Figure 1.2. As can be seen, a single wire is fed from a supply spool through a pulley and tension control unit to four wire guides. The SGS ingot on the holder is pushed down the wire web, which leads to material removal and slicing. This wire is under tension during cutting, and the apparatus provides different levels of force depending on the depth of the cut.

The wire is made of stainless steel and has a typical diameter of around 150-200 μm. The volume between the wire and the ingot surface is covered with a slurry containing abrasives such as SiC and diamond particles. The size of these abrasive particles

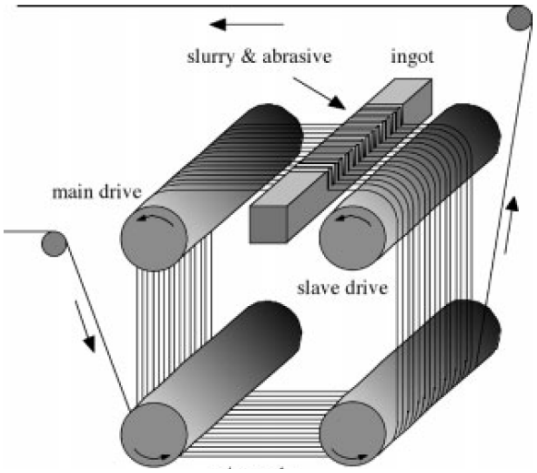

Figure 1.2: Wire Sawing Setup

are around 5-30 μm [30]. The slurry moves with the movement of the wire and acts as a transport medium for the abrasives into the sawing channels. The slurry must minimize the temperature rise during wire sawing by continually removing the heat of cutting. The actual material removed, also known as Kerf loss, is around 200-250 μm/wafer [30]. Since the wafer and the Kerf loss/wafer is almost same, it can be said that the Kerf loss represents nearly 50% of total wafer material. This wastage of material makes wire sawing an expensive method.

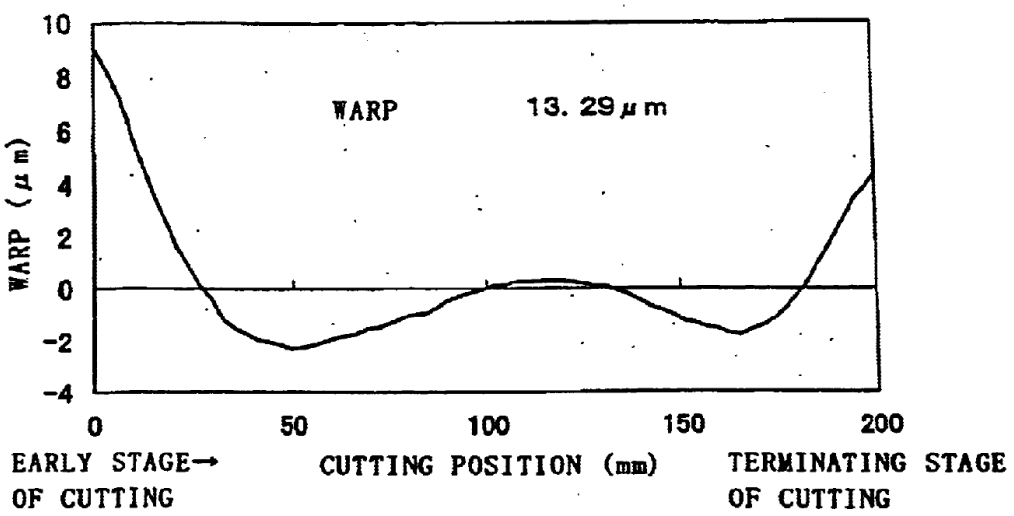

Figure 1.3: Warpage in wafers [2]

Although wire sawing is an efficient process, the wafer produced can be non-flat or warped, as shown in Figure 1.3. This can occur due to relaxation of pre-existing

stress within the ingot as well as thermal strains that develops during the sawing process. This warpage could be around 15 μm The uneven surface of wafers is an undesirable property as it leads to difficulty during fabrication process of solar cells. It is, therefore, important to optimize the sawing conditions to ensure a smooth wafer surface.

1.5 Summary

Wafers for solar cells are made from MGS material through a multi step process involving directional solidification of mc-Si ingots and wire sawing of these ingots. During these processes, defects such as warpage, dislocations, and residual stresses can be induced in the final wafer, which increases component costs and reduces the efficiency of the solar cells. In this thesis, a mathematical model for simulating the dislocation density, residual stress and warpage during Si processing is developed that can be used to understand the link between processing and solar cell wafer performance. In the next chapter, prior research conducted in the area of numerical simulation of directional solidification and wire sawing, along with the theories developed for predicting the thermoplastic behaviour of Si are reviewed.

Chapter 2

Literature Review

2.1 Introduction

Thermo-mechanical simulation of the multi-crystalline Si wafer fabrication process is a complex problem. This is due to the temperature dependent properties of Si and the large number of processing parameters involved in directional solidification and wire sawing. To perform such a task, therefore, sufficient knowledge of the physical and mechanical properties of Si, the directional solidification process, the wire sawing process, and finite element modelling are required. Hence, in this chapter, existing literature on these topics is reviewed. The literature review can be divided into three distinct areas: studies characterizing the (i) constitutive behaviour of Si, (ii) analytical and numerical studies of the directional solidification process, and (iii) analytical and numerical studies of the wire sawing process.

Experimental studies can be very informative in studying the evolution of the temperature and the mechanical state during thermo-mechanical processing of Si. However, experiments involving the directional solidification and wire sawing processes require considerable time and costs, so computational models have been developed to simulate the stress/strain and temperature fields under various cooling rates and material geometries (e.g. [12, 27, 28, 44]). These models were developed using numerical techniques such as finite element methods and require knowledge of the mathematical equations behind the physical processes. The validity of these models, however, needs to be tested against experimental data. These models can be very helpful to an industrial practitioner who wishes to improve product quality [12].

2.2 Si: Properties

2.2.1 Crystal structure and phases

Si is a covalently bonded material that exists as diamond cubic structure with a face-centered Bravais lattice and a two atom basis. Its lattice parameter is approximately 0.543 nm at 293 K [15]. Si displays allotropy, existing in different forms which have different lattice structures. These allotropes exists at different temperatures and pressures, and have different mechanical properties [20]. Pure Si crystal has a very high ductile to brittle transition temperature (DBTT); it is relatively brittle below 1073 K. However, under high stress during thermo-mechanical processing, Si can undergo allotropic transformation exhibiting ductility even below DBTT [20, 24].

2.2.2 Stress-Strain Behaviour

The stress-strain behaviour of single crystal Si is supplied as the input material property when performing any finite element thermo-mechanical simulation of Si processing. It is therefore important to understand the constitutive behaviour of this material. The stress-strain behaviour of Si has been thoroughly studied by several researchers, most notably by Patel [36] and Haasen, Alexander, and Sumino [1, 22].

Deformation tests have been performed to understand the plastic deformation of Si crystals at various temperatures and strain rates. These tests were conducted to characterize the various stages of single-crystal mechanical deformation. A typically observed stress-strain curve for Si is shown in Figure 2.1, demonstrating the behaviour at 1100 K. As can be seen, the stress-strain behaviour of single crystal Si consists of 5 distinct stages. In the first stage, at very low strains, the constitutive behaviour is bell shaped, [36], having upper and lower yield points. In the next stage, the stress-strain curve exhibits successive hardening and recovery behaviour, which are marked by an increase and a decrease in $d\sigma/d\epsilon$ values, respectively. These recovery and hardening stages occur at high strains as compared to the strains observed in

stage I. Therefore, when simulating a process in which Si crystal undergoes small deformation, such as casting, the stress-strain behaviour observed in stage I provides the relevant constitutive model. Note that the shape of the curve shown in Figure 2.1 is applicable over a wide range of temperatures above a homologous temperature of 0.6 [36].

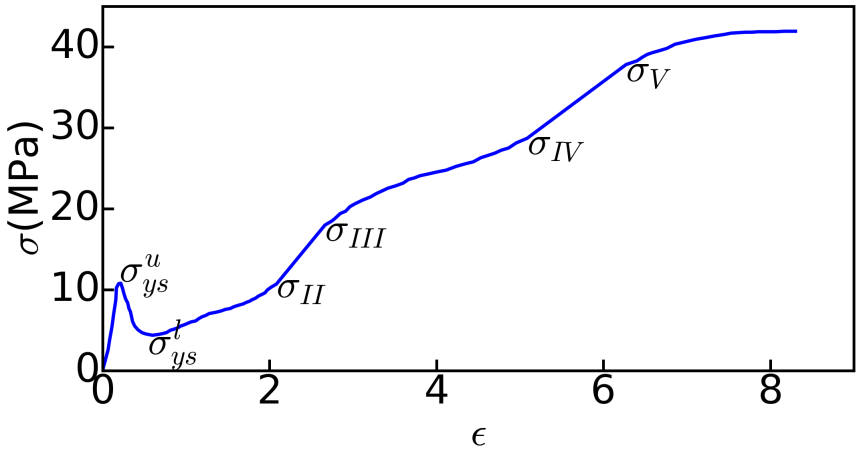

Figure 2.1: Stress-Strain curve of Si monocrystals with <123> orientation deformed in tension at T = 1100K and strain rate $\dot{\epsilon} = 2 \times 10^{-3} s^{-1}$ [40].

As shown in Figure 2.1, the evolution of the stress with respect to increasing strain is as follows. In stage I, the deformation is initially elastic, until the flow stress reaches an upper yield stress (σ^u_{ys}). Then, a sharp drop in the flow stress is observed until the flow stress reaches a lower yield point (σ^l_{ys}), and then it gradually rises again. The end of Stage I is identified by an increase in $d\sigma/d\epsilon$, indicating work hardening. The bell shape stress-strain curve that can be seen in the initial stages of deformation is a characteristic property of single crystal Si, however, the values of σ^u_{ys} and σ^l_{ys} change with temperature and strain rate [1, 50].

Hassan, Alexander and Sumino characterized the creep strain accumulation in single crystal Si with time under constant stress ($\leq$ 7 MPa) at high temperature ($T \geq 0.6T_m$, where T_m is the melting temperature). For metals, the inelastic strain accumulation with time under a load that gives no inelastic deformation at room temperature is called creep deformation. The time scale of creep strain accumulation is large. Normally, metals exhibit an inverted S shape creep curve, as shown in Figure

2.2. The creep curve consists of three zones. First, the transient creep stage. In this stage, the strain rate decreases continuously with time. Second, the steady state creep. In this stage, the strain rate is constant due to a steady state between recovery and hardening. Third, tertiary creep, in which the creep strain increases till material fractures.

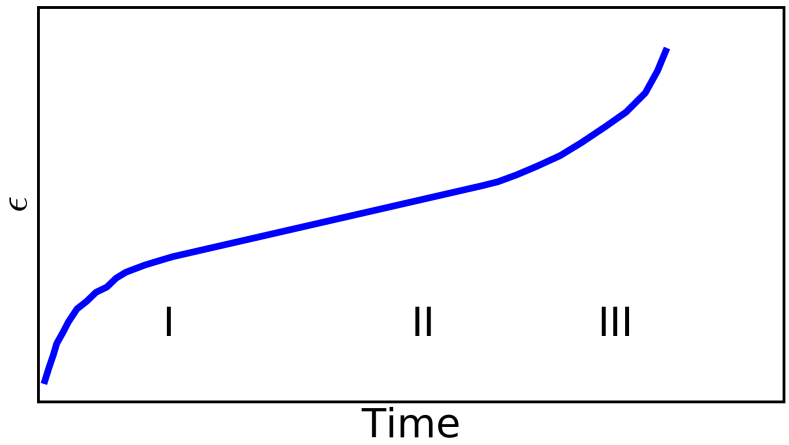

Figure 2.2: Creep curve for metals.

Based on their experiments, Hassan, Alexander and Sumino found that in single crystal Si, the inelastic strain with time was different than metal's in the initial transient phase. The transient creep curve was inverted, as shown in Figure 2.3. This transient creep phase had 3 zones. Incubation zone, stationary zone, and work-hardening zone. This inelastic creep strain accumulation was attributed to the observed decrease in yield point at σ_{ys}^{u} in Figure 2.1. The incubation zone was concluded to be present due to the initial rapid multiplication of dislocations. The stationary zone was characterized as the zone of inflection between the incubation and the work-hardening zone. In this zone the back stress for dislocation movement starts to increase till the dislocation movement finally starts to decrease. This decrease leads to the decrease in the strain accumulation rate which is characterized as the work-hardening zone. The creep curve eventually achieves a steady state and becomes independent of the dislocation density change. The relationship between dislocation kinetics and constitutive behavior in Si during stage I has been characterized as the well-known HAS model that links the dislocation multiplication rate dN_m/dt in time t with the dislocation

density and the dislocation velocity (and eventually shear strain via Orowan's law),

$$\frac{dN_m}{dt} = KN_m v \tag{2.1}$$

where K is a constant characterizing the dislocation multiplication rate, v is the velocity of the dislocations and N_m is the dislocation density.

It can be said that during the casting process of Si, the initial solid formed is dislocation free. Upon cooling, the thermal strains would develop which would lead to creep deformation. This creep would be transient, and proceed through stage I, II and III, shown in Figure 2.3. The dislocation density would increase until it reaches a steady state and the whole transient phase is complete. This is because the time scale of transient creep in Si in quite low compared to time scales of the casting process, allowing dislocation density to reach a steady-state and complete the full transient phase. In order to numerically simulate the Si casting process, it is therefore important to supply this transient constitutive behaviour to capture the creep strain accumulation.

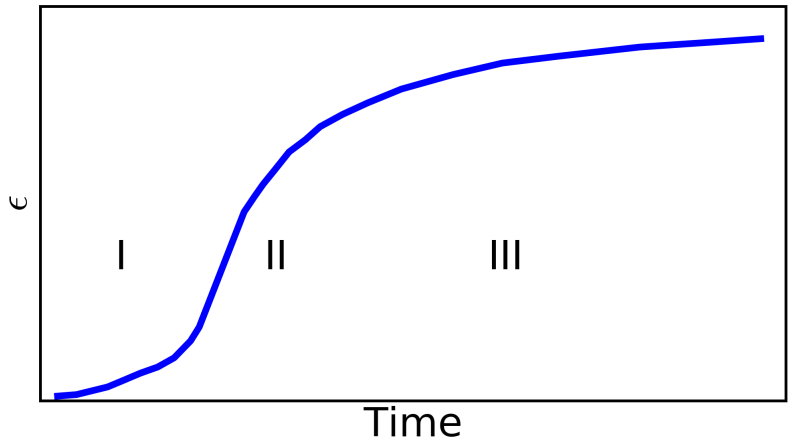

Figure 2.3: Creep curve for Si.

2.2.3 Constitutive Modelling Using Dislocation Multiplication

In any thermo-mechanical process, the total strain under the application of stress can be split into elastic and inelastic components. For small deformations, the rate of change of stress $\dot{\sigma}$ is proportional to the rate of change of elastic strain $\dot{\epsilon_e}$, which can be written as,

$$\dot{\sigma} = D\dot{\epsilon}_{el} = \mu(\dot{\epsilon} - \dot{\epsilon}_{ie}) \tag{2.2}$$

where D is the stiffness modulus, and $\dot{\epsilon}$, $\dot{\epsilon_{el}}$ and $\dot{\epsilon_{ie}}$ are total, elastic and inelastic strain rates, respectively. The stress-strain relationship shown in Equation 2.2 is macroscopic, and does not considers the underlying microstructural deformation mechanisms. In order to connect these two length scales, Orowan developed a set of equations to link inelastic deformation rate and the movement of dislocations,

$$\dot{\epsilon_{ie}} = bN_m\bar{v} \tag{2.3}$$

$$\bar{v} = k_0\sigma_{eff}^p exp(-Q/k_BT) \tag{2.4}$$

where $\bar{v}$ is the overall mean velocity of total dislocations N_m, k_B is the Boltzmann constant, T is the temperature, σ_{eff} is the stress available to increase the dislocation density, p is a fitting constant applied as power on σ_{eff} whose value was obtained as 1.1 for Si by Haasan [14], k_0 is a constant whose magnitudes have been found to be approximately 1 - 3.5 $\times$ 10^4 $\mathrm{m\,MPa^{-1}\,sec^{-1}}$ [16], and Q is the Arrhenius activation energy whose magnitude has been found between 2.20 - 2.35 eV [16]. The effective stress σ_{eff} in Equation 2.4, which is the stress available to multiply and increase the

dislocation density, is then written as,

$$\sigma_{eff} = \begin{cases} \sigma - D\sqrt{N_m}, & \text{if } \sigma > D\sqrt{N_m} \\ 0, & \text{if } \sigma \leq D\sqrt{N_m} \end{cases} \tag{2.5}$$

where N_m is the dislocation density, D is the strain hardening factor and σ is the applied stress. Note that, Equation 2.1-2.5, combined together, is referred to as the HAS model. This calculates the increase in dislocation density in a crystalline material, such as Si, as a function of applied stress. The reason for using σ_{eff} in Equation 2.4 instead of σ is because of the fact that the movement of dislocations is influenced by both the applied stress field and the increasing dislocation density. An increase in the dislocation density hinders the further movement and multiplication of dislocations. This hindrance can be incorporated as a back stress whose magnitude is a function of the current dislocation density. In the HAS model, this back stress is given as $D\sqrt{N_m}$. σ_{eff} can be positive or 0 depending on the value of dislocation density and equivalent stress. If σ_{eff} is 0 then, as shown by Equations 2.1 and 2.4, there is no change in dislocation density. With an increase in the dislocation density, the second term in Equation 2.5 increases, which leads to a decrease in σ_{eff} and, thus, a decrease in the dislocation multiplication rate. This further means that the largest increase in dislocation density will occur in the initial stages of deformation.

Computer based models developed to calculate the stress/strain state of a material, are provided with the relevant constitutive behaviour as input parameters. This constitutive behaviour is nothing but the value of stress σ as a function of various quantities such as strain ϵ, strain rate $\dot{\epsilon}$, temperature T, dislocation density ρ etc,

$$\sigma = f(\epsilon, \dot{\epsilon}, T, \rho, ..) \tag{2.6}$$

The accuracy of any developed model in terms of predicting the stress/strain state is dependent on the accuracy of the supplied constitute behaviour. The next

section reviews some of the past computer based models constructed to calculate the stress/strain state during casting of Si by using elastic-plastic and elastic-creep (HAS model) constitutive behaviour.

2.3 Numerical simulations of the Si casting process

Computational modelling of the constitutive behaviour of Si during casting has been performed by several researchers [7, 12, 26–28]. These models were developed to understand the residual stress and dislocation density in Si after casting for both electronic and photo-voltaic applications. These models were developed for various types of solidification processes including: Czochralski process [27], Float-zone process [32], Ribbon growth [21], Directional solidification [12, 17], and Electron beam remelting [26]. These models were developed either by applying a plastic constitutive behaviour or a dislocation creep behaviour.

For models using the plastic constitutive behaviour approach, the yield stress value is supplied in the form of flow curve data which is used to calculate the overall plastic deformation and thus the final residual stress. For models using the dislocation creep behaviour approach, an initial dislocation density is applied and the creep strain is then calculated during the process based on the HAS creep equation.

Over the years, many researchers have modified the original HAS creep equation to include the effects of grain boundary, impurities, and precipitates [7, 44]. The HAS creep equation has been applied either by assuming isotropy and using J2 based isotropic stress framework for dislocation growth [12, 27] or by assuming an-isotropy and applying a crystal plasticity framework [7, 29] to calculate dislocation growth along individual slip planes. In the next subsections, the various simulation models developed are reviewed and compared.

2.3.1 Plasticity-based Models

Plasticity based models apply the flow curve data while calculating the stress-strain state during any thermo-mechanical deformation process such as casting. These models calculate the residual stress in the Si ingot by applying the elastic and inelastic behaviour under the applied set of processing conditions. Maijer *et al* [26] developed a finite element model to investigate the residual stress distribution in mc-Si ingots during remelting and refining of electronic grade scrap Si to produce solar grade Si in an electron beam furnace. This process produces an ingot with columnar grain morphology having a radial orientation along the vertical sides of the ingot, and axial orientation along the bottom and center of the ingot. This complex morphology is present due to applied cooling conditions whereby heat is extracted from the side walls, bottom, and top of the ingot. The cooling boundary conditions were supplied to simulate temperature data during the cooling process, which was further validated against the actual temperature data obtained by measuring the furnace temperature at various locations below the ingot using thermocouples. Finally, the temperature data from the thermal simulation was used as the input parameters to predict the residual stress in the ingot. The input constitutive model, developed from flow stress data measured by Siethoff [42] did not contain any strain rate dependency. The predicted residual stress was validated [26] by comparing against results obtained from neutron diffraction measurements. This sequentially-coupled temperature-stress simulation was performed for various cooling conditions to study the effect of ingot withdraw rate and electron beam power on ingot residual stress. It was found that there were significant level of residual stress, on the order of 200 MPa, within the ingot, and neither the withdrawal rate nor the electron beam power had significant effect on this residual stress.

M'Hamdi *et al* [28] developed a finite element model to simulate the casting of mc-Si in a Crystalox DX-250 furnace. The simulation was carried out to investigate the stress buildup during directional cooling of mc-Si ingot. This furnace had insulated

side walls to facilitate directional solidification. The authors incorporated an elastic-visco-plastic constitutive model to calculate the final residual stress within the ingot. This visco-plasticity model was applied using a creep law developed by Widner and Rehwald [46], who observed that Si becomes a viscous material at high temperatures and its flow stress depends on both temperature and strain rate,

$$\sigma_s = \sigma_0 \exp\left(\frac{-\triangle E}{k_B T}\right)\left(\frac{\dot{\epsilon}}{\dot{\epsilon}_0}\right)^{1/n} \tag{2.7}$$

where σ is the Mises stress in Pa, $\dot{\epsilon}$ is the strain rate, $\dot{\epsilon}_0$ is a reference strain rate equal to 10^{-3} s^{-1}, $\triangle E$ is the activation energy for the movement of dislocation, k_B is the Boltzman's constant, and T is the temperature in K. Note that σ_0, E, and n are the material-dependent properties. Different values of these variables have been proposed by various researchers [36, 41, 50] through experiments. This equation is independent of time, which means it represents a Si steady state creep assumption rather than a transient creep assumption.

The residual visco-plastic strain predicted by M'Hamdi *et al* [28] using this creep constitutive behaviour demonstrated the effects of thermal gradient on inelastic deformation during directional casting of Si. Based on this simulation, the cooling conditions were optimized to minimize the visco-plastic strain in the ingot. This model, however, does not predicts the final dislocation density distribution. Simulating dislocation density can assist in further process optimization as it can help to understand the evolution of dislocations, the root cause of residual stress under the applied processing conditions.

2.3.2 Dislocation creep based Models

Several researchers have developed computational models to simulate dislocation density and residual stress during casting based on the HAS model and then successfully validate them. These simulations have been developed for different types of Si casting processes including Czochralski process [27], Ribbon growth [21] and Directional

solidification [12, 17]. Use of the HAS equation coupled with process specific stress and thermal conditions has led to optimization of these processes to decrease the dislocation density in the product.

Maroudas and Brown [27] were among the first to develop and validate a HAS creep based computer simulation model for dislocation growth in Si during solidification. They performed the simulation for the Czochralski and liquid encapsulated Czochralski processes. Both are methods to produce single crystal Si, with the second one producing larger diameter ingots by covering the top of the Si melt with an encapsulant such as Boric acid to prevent Si oxidation.

Maroudas and Brown coupled the HAS equation with the geometry, pull rate, and stress, and predicted a final dislocation profile in the ingots. They validated this density against the etch pitch density data [19]. It was found that the predicted data was in close agreement with the etch pit data for the case of liquid Encapsulated Czochralski process but not for the Czochralski process. This inaccuracy was attributed to the fact that the HAS model is dependent on initial dislocation density and in the Czochralski process, there are very small number of initial dislocations. The conclusion based on this work was that HAS model is good for predicting plastic relief due to increase in dislocation density in the bulk but it cannot explain the dislocation formation from the melt at the solid-liquid interface during solidification.

Franke *et al* [12] carried out a finite element simulation to reduce the dislocations in mc-Si ingots produced by Deutsche Solar via the SOLSPIN process. This process is based on the principle of directional solidification and designed to maintained a planer solidification front by supplying proper insulation and controlling the crystallization velocity. The simulation was carried out to predict the dislocation density growth for a cuboid geometry. In this simulation, a thermal model based on the cooling data collected from the furnace was developed followed by development of HAS creep coupled stress-strain model. Based on the predicted dislocation growth profile from these simulations, the cooling process was categorised into 3 phases as shown in Figure 2.5. During the first phase, which was just after liquid to solid phase change, a strong

increase in dislocation density was found. This was attributed to the strong thermal gradient present at the solid-liquid interface required to propagate solidification. In the second phase, the dislocation growth was observed to occur in steps due to the thermal gradient from the lack of control in the insulation power of the furnace. The third phase was observed below 800°C in which dislocation density remained constant. The results of this simulation were used to optimize the process parameters to reduce the dislocation growth in phase 1 and 2 which led to a 0.5% increase in the efficiency of final wafers made from these ingots.

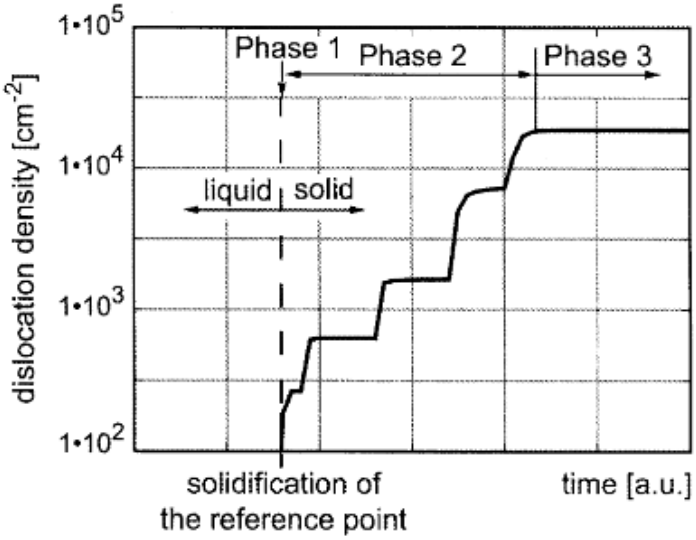

Figure 2.4: Dislocation growth in SOLSPIN process simulated by Franke *et al* [12] showing the growth of dislocation in steps.

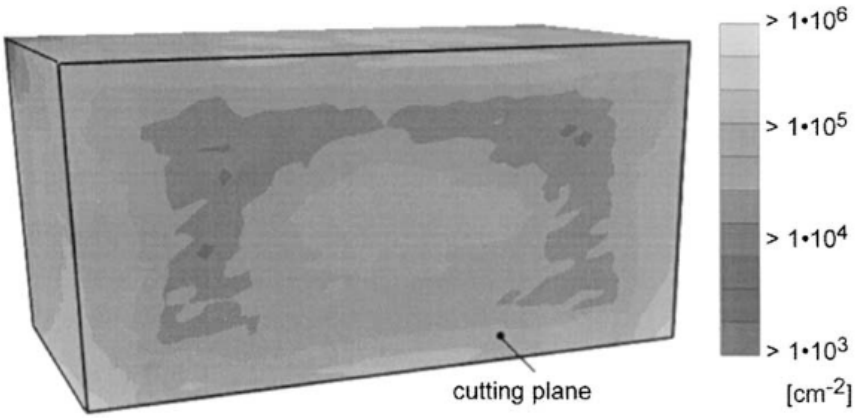

Figure 2.5: Dislocation profile in SOLSPIN process simulated by Franke *et al* [12] in the central plane of the ingot.

Nakano *et al* [17] have performed a HAS model based simulation to predict the dislocation density in unidirectional solidified mc-Si ingots under various cooling rates. The results of this simulation showed that a faster cooling rate led to a higher dislocation density and a higher residual stress. In all cases, there was no dislocation increase below 900 K. Based on the final distribution of residual stress and dislocation density, it was found that regions with a higher dislocation density also had a higher residual stress as shown in Figure 5.10. This was attributed to the fact that the thermal strain relaxation due to dislocation multiplication and movement selectively occurred at some areas upon cooling, this led higher residual stresses.

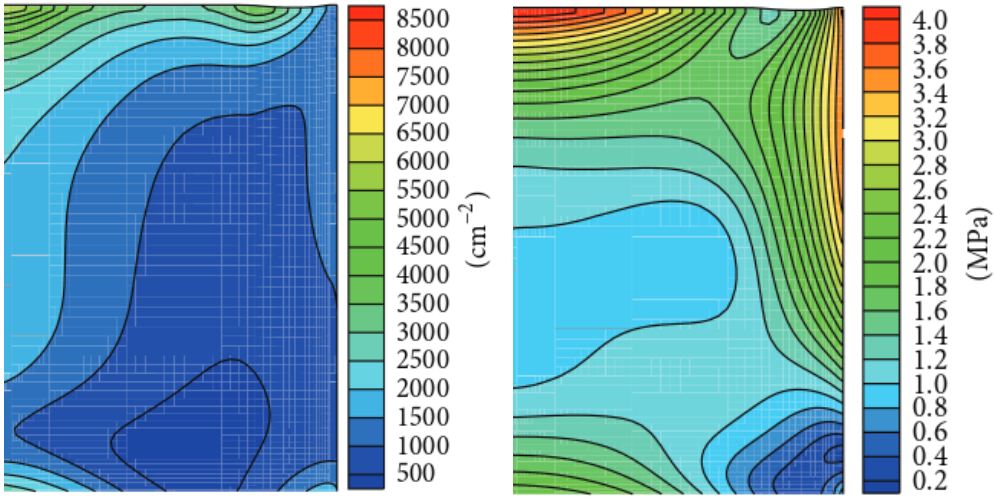

Figure 2.6: Dislocation density (Left) and residual stress (Right) profile in half of directionally solidified mc-Si ingot cooled at 5 K/Min [17]

The models discussed above have an underlying assumption that the material properties are isotropic. Under this assumption, equivalent Von Mises stress, as per J2 plasticity, is supplied as the value of stress in the HAS equation. However, it is well known that single crystal Si and highly directional columnar grains are strongly anisotopic. Several researchers have developed anisotropic forms of the HAS equation. In studies by Miyazaki [29] and Cochard *et al* [7], the HAS equation was applied on all 12 slip planes of Si assuming FCC crystal structure, and also by accounting for plasticity due to inter-slip plane dislocation interactions, otherwise known as latent hardening. The results of these simulation have been shown to be more accurate and show more insights as compared to a Von Mises implementation of HAS model for

such cases with highly anisotropic or directional property [7].

2.4 Wire Sawing

Wire sawing is a complex process, with several processing factors and parameters, as summarised in Table 2.1. Wafers produced from wire sawing suffer from several problems, including surface cracks [47], warpage [49], and non uniform thickness [51] . Therefore, analytical and numerical models of this process have been developed to quantify the effects of various processing conditions on the wafer quality [30, 47].

Table 2.1: Wire sawing processing parameters

Factors	Parameters
Wire	Tension, Velocity, Diameter, Vibration
Slurry	Viscosity, Heat Transfer Coefficient
Abrasives	Density, Shape, Size
Work-piece	Mechanical Properties, Pre-stresses, Inclusions

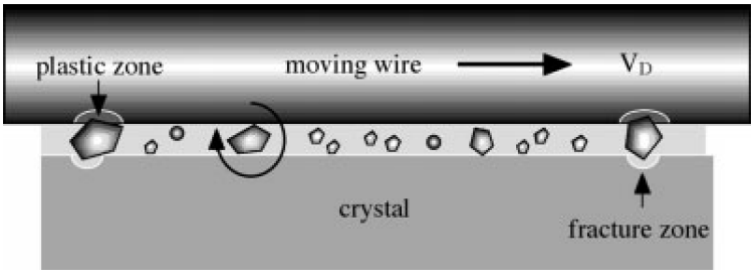

Figure 2.7: Movement of abrasives with wire

The basics of wire sawing were discussed in section 1.4. As mentioned earlier, wire sawing involves cutting of Si ingot by abrasive particles moving with the movement of a slurry due to the torque provided by the rotation of wire. This is shown in Figure 2.7. Si is a brittle material around room temperature, and undergoes cutting due to the propagation of cracks developed by the indentation of abrasives on the work-piece. During this process, due to high stress concentration near the crack, there is plastic deformation also. Moller *et al* [30] have developed a model of material removal through crack propagation using fracture mechanics. They have incorporated the effects of wire parameters on the material removal rate. Li *et al* [23] developed a

model to understand the affects of abrasive shape on the stress developed during the cutting process. Bidiville *et al* [5] have shown that smaller abrasive particles lead to fewer cracks on the surface and better wafers. Du *el al* [11] have reported that mc-Si ingots grown from directional solidification contain SiC and Si_3N_4 inclusions which lead to non-smooth wafers.

Unequal thermal expansion and thermal strain at different locations on the wafers during the cutting process can lead to warping (bending) or breaking of the wafers. Ariga *et al* [2] and Lundth *et al* [25] have measured temperature gradient of around 20-40 °C between the middle and the end of the wafer. Bhagavat and Kao [4] have developed a finite element model to simulate the temperature rise during wire sawing. The heat flux entering into the work-piece from the wire and the natural convection through the new surface formed was applied as boundary conditions to generate this temperature profile. They have also suggested an intelligent control of boundary conditions to keep the work-piece always close to the room temperature. This can reduce the warpage in wafers by keeping the thermal gradient low. They have also claimed the predicted temperature profile to be in close agreement with the experimental temperature profile from Ariga *et al* [2] and Lundth *et al* [25] as shown in Figure 2.8.

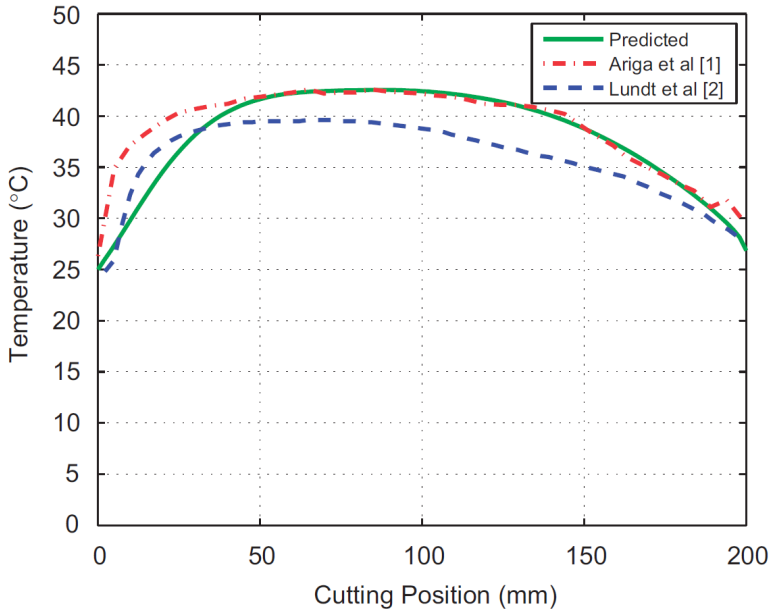

Figure 2.8: Temperature profile predicted by Bhagavat & Kao [4] during Wire Sawing

Yamada *et al* [49] have developed a finite element model to calculate the warpage in wafers during wire sawing. They predicted a warpage of 6-7 μm which although was in good agreement in magnitude with the experimental warpage, occurred at different locations. It should be noted that this prior work only considered thermal expansion as the factor contributing to warpage and not the plasticity induced at crack tip from abrasives. This paper also did not explicitly define the constitutive behaviour model used for Si.

Moller *el al* [30, 31] have developed several models to relate the material removal with cutting speed and wire load based on the indentation created by particles on the surface of the ingot. The amount of indentation was determined to be dependent mainly upon the density of abrasive particles touching Si. Material removal occurs by the propagation of the cracks developed from indentations. The material removal rate v_s as per their model can be written as,

$$v_s = \frac{m \;\; V_0}{A_s \; \triangle t} \tag{2.8}$$

where m is the indentation events per unit contact area A_s in time $\triangle t$ and V_0 is the material removed per indentation event. Based on indentation and fracture mechanics, V_0 has been found to be a function of the normal force from the wire F_N acting on the work-piece, and given as,

$$V_0 = F_N^{2.2} \tag{2.9}$$

As per Equation 2.8, it is clear that the material removal rate is inversely proportional to the wire-workpiece contact length. This means that the time taken for the successive removal of layers of Si during cutting is dependent on the work-piece geometry and is different for a cylindrical and a cuboid work-piece.

2.5 Summary

Themo-mechanical simulations are useful in predicting the final properties of material after processing. In this chapter, some of the models developed to predict the properties of mc-Si ingots and wafers for photovoltaic applications have been briefly discussed. This discussion covers past models developed using two approaches: elastic-plastic approach, and elastic-creep (dislocation) approach.

In the first class, research by Maijer *et al* [26] and M'Hamdi *et al* [28] were presented. The results of these models are in good agreement with the measured values of residual stress/strain. However, they could be further modified to predict the dislocation density. The next class of models discussed were the ones based on the HAS analytical model [1, 14, 43] of single crystal Si. This model was developed using the observed stress/strain curve of single crystal Si and it explains the effects of temperature, stress and strain-rate on constitutive behaviour. This analytical model has been used by several researchers, including Mouradus and Brown [27], Franke *et al* [12], Cochard *et al* [6], and Ioune *et al* [17], to numerically simulate the dislocation density during the solidification of Si, both single and multi crystalline. These models have predicted the final residual stress and dislocation density after solidification. Since these models predict the inelastic strains (due to dislocation growth) based on the cooling rate, they have been exploited industrially to optimize the cooling conditions that produce mc-Si ingots with lower dislocation density. However, the problem with these models lies in the over-simplification in the assumptions that are taken. One such assumption was isotropy, which is not the case in case of a single crystal Si and directional solidified metals in general. The influence of grain-boundary and precipitates/inclusions on the dislocation behaviour was also ignored in these model. Other researchers have also questioned the accuracy of dislocation predictions using the HAS models in mc-Si ingots during directional solidification. For example Ryningen *et al* [37] experimentally argued that stress based models are not very accurate in predicting the dislocation density and the dislocation growth is a local phenomenon affected

by the grain boundary and crystal growth.

The chapter further discussed the wire sawing process and some of the works carried out by Mollner *et al* [3, 4, 30, 31] to understand the underlying processes during wire sawing and their affect on the wafer quality. While these works cover the effect of wire, abrasives and slurry, they do not incorporate the effect of initial residual stress in the work piece (ingot). Furthermore, it was found that currently there is only one thermo-mechanical simulation [49] performed to measure the warpage of wafers during wire sawing. This may be because, predicting the wafer warpage would require both the modelling of directional solidification and wire sawing process. Plasticity during wire sawing is a complex phenomenon and comes from two sources. First, the abrasives act as indentors and lead to plastic deformation. Second, the plastic deformation due to thermal strain and temperature gradient during this process. These plastic deformations are interesting problems to address, however, for this study only the plastic deformation from the later factor is considered.

Chapter 3

Scope and Objectives

3.1 Scope of this Research Work

In recent years, wafers for solar cells have been produced by wire sawing of directionally solidified mc-Si ingots. The wafers produced in this way have two issues. 1. Loss of efficiency due to the presence of defects such as dislocations, impurity atoms and grain boundaries. 2. Warpage in wafers during wire sawing due to inelastic deformations and the presence of initial residual stress in the work piece i.e. directionally solidified mc-Si ingots.

Over the years, a number of finite element models have been developed for predicting dislocation growth and residual stress during the directional solidification process of mc-Si ingots. These models take into account the dislocation kinetics model of Si. When it comes to wire sawing, however, there are limited finite element models available for predicting warpage and residual stress. For the thermal simulation, only Bhagavat and Kao [4] have developed a FE model, to the best knowledge of the author and for the stress simulation, a few analytical models have been developed [30, 31]. Furthermore, the author could not find any models that considers the effect of pre-existing residual stress and dislocation density in the work-piece on the wafer quality.

3.2 Objective of this Research Work

The goal of this work is to simulate warpage in wafers as-cut from directionally solidified ingots. To perform such a simulation, a finite element model is developed both

for the directional solidification and wire sawing processes, with the later taking the results of the former as initial conditions. Furthermore, to study the effects of cooling conditions during solidification, simulations are performed for cooling rates of 2, 5 and 8 K/Min i.e. slow, medium and fast cooling respectively. The current work can be broken down into 3 steps, as shown in Figure 3.1,

(1). Thermal and stress simulation of DS process: Casting Model

(2). Post-processing/mapping of results from casting model on a wire sawing simulation mesh

(3). Thermal and stress simulation of wire sawing process: Wire-sawing Model

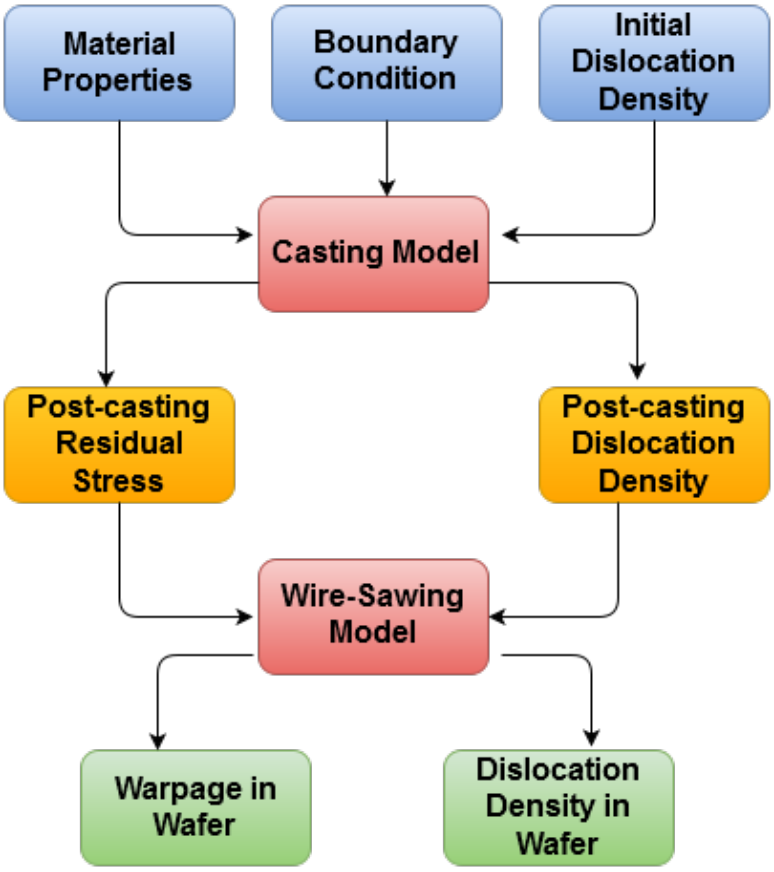

Figure 3.1: Overview of the simulations

Chapter 4

Model Development

4.1 Introduction

In this thesis, the objective is to develop a numerical model to simulate the residual stress and dislocation density distributions found in Si wafers produced for solar cell applications. The manufacturing process involves casting via directional solidification and then wire sawing. Both process steps involve significant thermal loads and mechanical deformation. In order to determine the material state after wire sawing, it is necessary to simulate both the evolution in temperature and in stress/strain state. However, solving these equations is challenging because they require accurate material properties, boundary conditions, geometry and state equations (for stress and dislocations). These material properties can vary significantly depending upon the purity and grain structure of Si. The boundary conditions and geometry can vary depending on the physical setup for which the process is being simulated.

Mathematical equations for any physical process, such as temperature evolution and mechanical deformation, can be solved using numerical methods. One of the most commonly used numerical methods for solving problems related to continuum mechanics is the finite element analysis (FEA). In this research project, the commercial finite element software package ABAQUS 6.12 has been used to model the processing of Si wafers. This software is an efficient explicit/implicit finite element simulation package with excellent capability to solve transient heat transfer problems and mechanical deformation problems, and is very well documented.

4.2 Model Formulation, Domain & Geometry

4.2.1 Analysis Formulation

The finite element prediction of the residual stress and dislocation density after directional solidification and wire sawing requires solving the heat transfer and stress-strain partial differential equations. The heat transfer equation during solidification is simplified by neglecting convection; heat conduction is assumed to be the only heat transport medium. The heat transfer equation in the standard form used in the finite element formulation is given by,

$$\frac{\partial(\rho c_p T)}{\partial t} - \nabla \cdot (k \nabla T) = \dot{Q} \tag{4.1}$$

where ρ is the density in $\mathrm{kg\,m^{-3}}$, c_p is the specific heat in $\mathrm{J\,kg^{-1}\,K^{-1}}$, T is the temperature, k is the thermal conductivity in $\mathrm{W\,m^{-1}\,K^{-1}}$, and $\dot{Q}$ is the heat generated inside the domain in $\mathrm{W\,m^{-3}}$. In the case of a thermal model simulating solidification, the term $\dot{Q}$ represents the latent heat. This equation is discretized and then solved to obtain the evolution in temperature across the domain.

The main stresses during casting and wire-sawing arise from thermal strains that occur as a result of temperature variations across the domain (if the pressure from the wire is ignored). These thermal strains are then used to calculate the residual stress and dislocation density. The governing equation defining this problem is the equation of stress, given by,

$$\nabla \cdot \sigma_S + b = 0 \tag{4.2}$$

where σ_S and b represent the stress and the acting body force at any point inside the domain respectively. The stress in this equation can be further written in terms of the displacement or the strain via the material constitutive equation and Hooke's law. This displacement can then be solved numerically, with the supplied body force

and displacement boundary conditions.

If the strains are small, and deformation is within the elastic regime, then the stress tensor (σ) and the strain tensor (ϵ) have a linear dependence proportional to a stiffness matrix $[D^{el}]$ as per Hooke's law,

$$(\sigma) = [D^{el}](\epsilon^{el}) \tag{4.3}$$

where the matrix $[D^{el}]$ contains the material elastic constants that are a function of elastic modulus and Poissons ratio. Beyond the elastic regime, the relation between stress and strain is no longer linear and thus $[D]$ depends upon the respective constitutive behavior of the material. In a finite element analysis, this is simulated incrementally, i.e.,

$$d\sigma = D^{in} d\epsilon^{in} \tag{4.4}$$

where $d\sigma$ and $d\epsilon$ represent the increment of stress σ and strain ϵ, respectively and $[D^{in}]$ represents the inelastic constitutive behaviour of the material.

The ABAQUS software contains four built-in constitutive models: elastic-plastic, elastic-viscoelastic, elastic-creep and elastic-creep-plastic. As discussed in the literature review, the constitutive behaviour of Si during casting and wire-sawing is mainly governed by dislocation creep deformation, and so the elastic-creep ABAQUS scheme is used in this thesis. A custom subroutine has been written in FORTRAN 77 to implement the dislocation creep model. This will be discussed later-on.

Within ABAQUS, thermal-mechanical FEA can be performed in one of two ways. First, known as fully-coupled analysis, the heat transfer and stress-strain equations are solved simultaneously. Second, known as sequential coupling analysis, the heat transfer equation is solved first and its results are then applied as boundary conditions to the mechanical model when solving the stress-strain equations. The first option is used when the heat transfer and the stress-strain equations have a strong mutual dependence. The second option is used when the interaction can be approximated

as one way i.e. while the stress-stress equation is dependent on the heat transfer equation, the inverse is not the case.

In finite element methods, the correctness of a solution is determined by the size of the residual values (residuals are mathematical functions of the independent variables, temperature and stress in this case). In a transient coupled thermo-mechanical analysis, at each time increment, ABAQUS iteratively calculates the values of stress and temperature to minimise the value of the residuals. Mathematically, the fully coupled analysis can be written as,

$$\begin{bmatrix} K_{uu} & K_{uT} \\ K_{Tu} & K_{TT} \end{bmatrix} \begin{pmatrix} \nabla u \\ \nabla T \end{pmatrix} = \begin{pmatrix} R_u \\ R_T \end{pmatrix} \tag{4.5}$$

where ∇u and ∇T are the respective corrections to the incremental displacement and temperature, K_{ij} are components of the unsymmetric Jacobian matrix and R_i are mechanical and thermal components of the residual vector. ABAQUS solves this coupled system using the Newton-Raphson method with the heat transfer and the strain-strain differential equations solved using a backward-difference scheme.

In case of a weak coupling or a sequentially coupled analysis, the off-diagonal submatrices K_{uT} are K_{Tu} are small compared to the components in the diagonals in the Jacobian matrix of Equation 4.5. The off-diagonal components can be set to 0 as shown,

$$\begin{bmatrix} K_{uu} & 0 \\ 0 & K_{TT} \end{bmatrix} \begin{pmatrix} \nabla u \\ \nabla T \end{pmatrix} = \begin{pmatrix} R_u \\ R_T \end{pmatrix} \tag{4.6}$$

Due to this approximation, the thermal and the mechanical equations can be solved separately and more efficiently, reducing computation time.

In this project, sequential coupling is applied. The main issue with this approach is the need to take extra precautions while solving the stress-strain equations since the stress fields, which are linked to the generation of dislocations, are very sensitive to temperature changes. Under such temperature-dependent kinematical framework,

even a small error in the temperature field might introduce large errors in the stress-strain fields and hence a high level of accuracy in temperature is required. In this work, errors in the temperature are minimized by enforcing a maximum time steps of two seconds in the thermal model. As will be discussed later, two seconds is small in comparison with the total casting simulation time. The use of a small time-step considerably increases processing time but ensures accuracy. The overall temporal discretization scheme was implicit.

4.2.2 Model Domain, Geometry and Meshing

Casting

The geometry used to simulate mc-Si casting was cylindrical, to match a Crystalox DX-250 furnace found in the literature, with dimensions 250 mm in diameter and 105 mm in height [28]. The goal was to characterize the thermal evolution of the ingot during directional solidification, along with the residual stress and dislocation density states at the end of the casting process. Due to symmetry along the centreline, finite element analysis is only required for a one-half radial section having dimension of 125 mm by 105 mm. Further, the geometry allows the simulation to be converted from 3D to axi-symmetric, saving computational time. The geometry was meshed with 1548 nodes and 1470 elements with each element having four nodes. The element types used for thermal and stress models were axisymmetric diffusive heat transfer and axisymmetric reduced-integration given by DCAX4 and CAX4R respectively in ABAQUS. The domain is shown in Figure 4.1.

The objective of this analysis was also to study the residual stress and the dislocation density under a range of cooling rates. These cooling rates were simulated by assuming the bottom surface to cool at 2, 5 and 8 K/Min, mimicking slow, medium and fast cooling respectively. The time supplied for simulation was 900, 300 and 200 minutes respectively for slow, medium and fast cooling. Extra time was supplied in these simulations to ensure that the entire domain cooled to 298 K.

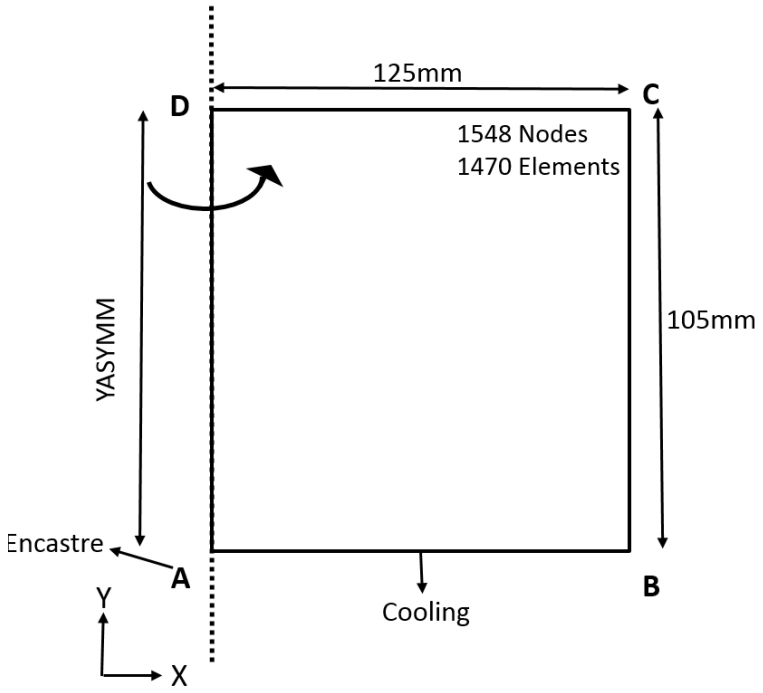

Figure 4.1: Mesh for casting simulation

Wire Sawing

The analysis domain for the wire sawing model was a circular volume with diameter 250 mm and height 1500 μ m. The goal was to determine the variation in warpage and dislocation density in as-cut Si wafers taken from different heights along the ingot after the cutting process. The wire sawing simulations were performed on three different locations within the casting: 26.25, 52.5, and 79.75 mm from the base of the ingot. The reason for performing the analysis on these sections instead of the whole ingot was to minimize computational cost and time. The caveat of this approach is the need to correctly map stress, strain and dislocation density from the casting model onto these sections. The first step was to map the stress, displacement, and dislocation density fields from the results of the casting simulation as initial conditions. Once mapped, thermal and mechanical simulations were performed. For all the three sections, only a single thermal model was built because it was assumed that the temperature profile while multi-wire sawing does not vary along the axis of the ingot. The mechanical models were built separately for these three sections, and applied the temperature

results from the thermal simulation of wire sawing as a pre-existing field. The time for wire sawing was taken as 400 minutes following industry standard practise [4, 49].

An axisymmetric mesh could not be used for modelling wire sawing because it is not a symmetric operation. A special type of mesh, as shown in Figure 4.2, was constructed by writing a script in PYTHON. This mesh had parallel lines perpendicular to the feed movement direction. This meshing was used to simulate a material removal pattern with wire movement from the entry point to the exit point. Note that this mesh is still an approximate representation of the wire sawing since in reality the wire bows during this process. This mesh had 9608 nodes and 6903 elements with 8 nodes per element for both the thermal and stress models. The 3D diffusive heat transfer DC3D8 and continuum C3D8 elements were used for the thermal and mechanical, respectively, models.

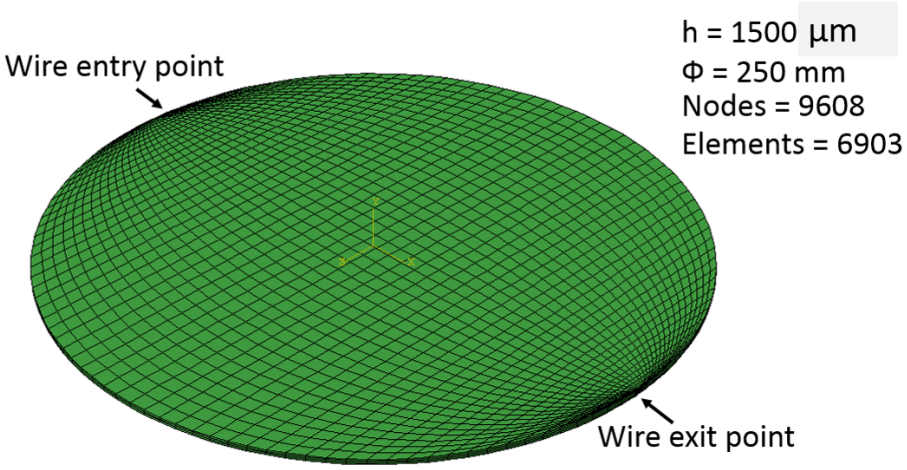

Figure 4.2: Mesh for wire sawing simulation

4.3 Input Material Properties

4.3.1 Thermal Properties

The thermal properties of liquid and solid Si, required for performing the temperature finite element analysis, include: density, latent heat of fusion, heat capacity, and

thermal conductivity. These are tabulated along with their respective sources in tables 4.1-4.3. Impure materials usually solidify over a temperature range, between the liquidus and solidus. The size of this range depends upon the concentration of primary and secondary constituents in it. For a material with a high concentration of one constituent, the liquidus-solidus range is small. During directional solidification of mc-Si from MGS, due to the 98% purity of Si, this range is between 0.5-1 K around the melting point temperature i.e. 1683 K. The thermal conductivity and the heat capacity of Si depends on temperature [13] and change significantly from room temperature to its melting point.

Si, unlike other elements, is unique in that the density of the liquid is greater than the solid, by about 9-10% [12, 26]. This implies that solid Si has the potential to float during solidification. However, for this analysis, this material behavior is ignored to reduce complexity. The variation in density with temperature for solid Si is also ignored because adding that feature would change the mass balance of the system. If there is no mass leaving or entering the domain, then a change in density implies a change in volume. To accommodate this volume change, the meshing needs to change. In order to prevent this complexity, the density is assumed constant.

Table 4.1: Thermal property of Si [28]

$T_{solidus}$ (K)	1682.5
$T_{liquidus}$ (K)	1683
Latent Heat, L ($\mathrm{kJ\,kg^{-1}}$)	1926
Density, ρ ($\mathrm{kg\,m^{-3}}$)	2330

4.3.2 Mechanical Properties

The mechanical properties required for performing the stress/strain finite element analysis are: elastic moduli, Poissons ratio and thermal expansion. These properties are tabulated in table 4.4, along with their respective sources.

Table 4.2: Thermal Conductivity of Si with Temperature [13]

T (K)	k ($\mathrm{W\,m^{-1}\,K^{-1}}$)	T (K)	k ($\mathrm{W\,m^{-1}\,K^{-1}}$)
200	266	1000	31
300	156	1100	28
400	105	1200	26
500	80	1300	25
600	64	1400	24
700	52	1500	23
800	43	1683	22
900	36	1684	100

Table 4.3: Specific heat of Si with Temperature [35]

T (K)	C_p ($\mathrm{J\,kg^{-1}\,K^{-1}}$)	T (K)	C_p ($\mathrm{J\,kg^{-1}\,K^{-1}}$)
293	657	975	920
370	735	1079	935
447	790	1156	944
474	805	1281	963
535	831	1398	980
570	844	1481	989
666	870	1614	994
772	889	1656	994
874	904	1800	989

Table 4.4: Mechanical property of Si [28]

Property	Temperature range (K)	Value
Thermal Expansion Coefficient $\alpha'(T)$ ($\mathrm{K^{-1}}$) [34]	$298 < T < 1683$ $1683 < T$	$3.725\times10^{-6} \cdot [1 - e^{b}]$ $b = -5.88(T - 124)10^{-3} + 5.55T10^{-4}$ 0
Young's Modulus E (Pa)	$298 < T < 1683$ T = 1713 T = 1773	$1.7 \times 10^{11} - 2.771 \times 10^{4} \times T^{2}$ 100 1
Poisson's Ratio ν	N/A	0.22

Elastic modulus:

The elastic modulus is a function of temperature, changing from 167 GPa at room temperature to 91 GPa at the melting point. Above the melting point, it is ramped down to a significantly lower value over the next 50 K. This was done to ensure that the liquid transitions into the a solid without experiencing sudden deformation that may lead to inelastic strains.

Coefficient of thermal expansion:

Although the actual coefficient of thermal expansion is given in table 4.4, ABAQUS requires this information in a format known as total thermal expansion based on a reference temperature as shown in Equation 4.7.

$$\alpha(T) = \frac{1}{T - T^0} \int_{T^0}^{T} \alpha'(T) dT \tag{4.7}$$

where α is the effective thermal expansion, α' is the temperature dependent thermal expansion coefficient, as given in Table 4.4 and T^0 is the reference point specifying the critical temperature where it is assumed that the material has zero thermal strain. In this study, T^0 was taken to be the melting temperature of Si, 1683K, since in molten form there is no strain. The total thermal expansion α can be imagined as the average rate of change of length with temperature rather than instantaneous rate of change between the reference and current temperatures.

Stress - Strain data:

In this analysis, the elastic-creep behavior governed by the HAS creep model is considered. These governing equations are further discussed in the literature review. The inelastic deformation occurs to compensate for the movement and multiplication of dislocation.

4.4 Initial & Boundary Conditions

4.4.1 Casting: Thermal Model

The initial condition for the thermal model was the initial temperature of the Si melt, and this was assumed to be 1773 K. This is the maximum temperature that the Si reaches in the furnace prior to the start of the solidification process. Thermal boundary conditions were placed on all edges of the mesh shown in Figure 4.1. Specifically, the edges BC & CD are assumed to be insulated, while it is assumed that heat is extracted through the bottom edge AB. A special convective boundary condition was applied to approximate a Dirichlet BC in order to achieve cooling rates of 2, 5, and 8 K/min on edge AB A Dirichlet boundary condition in heat transfer physics is a prescribed value of temperature on the boundary. This could be a constant value or some predefined function. It can be written as,

$$T = f(t) \tag{4.8}$$

where, T is the boundary temperature and $f(t)$ is a function in time t. In finite elements, Dirichlet boundary conditions often pose convergence difficulties. To avoid these issues, a special convective boundary condition/surface film coefficient was developed in ABAQUS in which the sink temperature was ramped down from 1773 K to 298 K at 2, 5 and 8 K/Min and the film coefficient was assigned a large value so that the nodes at surface AB always remain at the sink temperature.

4.4.2 Casting: Displacement Model

Mc-Si ingots are observed to have an initial homogeneous dislocation density of $1-100$ cm^{-2} [33], hence this was chosen as an initial condition for dislocation density field. During the displacement simulation, temperature data is read from the thermal model as a pre-existing condition at each increment. This data was read from the thermal model result database using ABAQUS inbuilt functions.

Mechanical boundary conditions were supplied to ensure that the nodes on the edges move within the physical movement space available during the solidification process. The nodes on the edge BC cannot move outwards, but since it is known that Si contracts during cooling from high temperature to low temperature, nodes on edge BC were not constrained mechanically. The node at A was mechanically pinned to ensure that at least one point on the edge AB stays in contact with the bottom. This leaves other nodes on edge AB free to move.

In addition to the above boundary conditions, the nodes on the edge DA were constrained to move only in the vertical direction Y. This was done to ensure that the mesh respects the symmetry of the physical space and the nodes on edge DA do not move radially since this would mean that the ingot is tearing from the center.

4.4.3 Wire Sawing: Thermal Model

An initial temperature of 298 K, representing room temperature, is applied to all of the nodes of the wire sawing mesh. The system is then allowed to heat up.

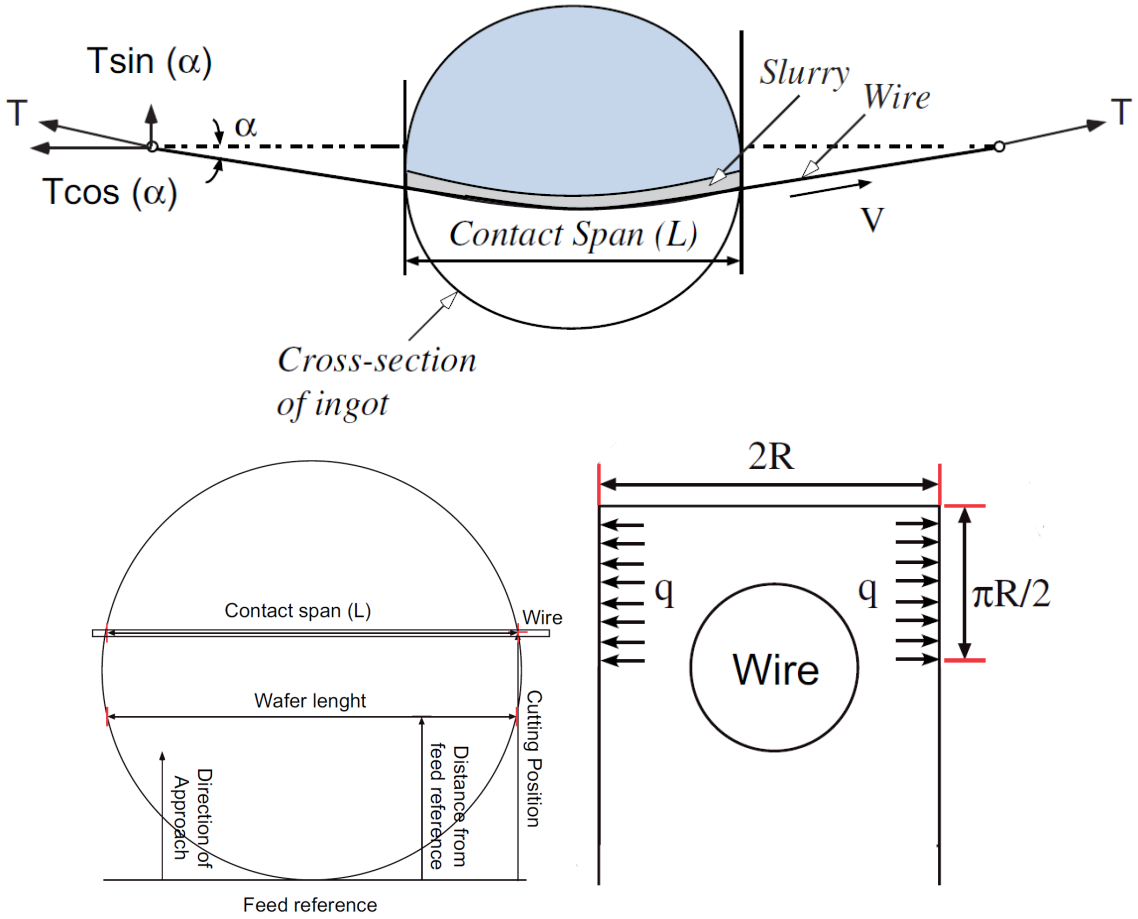

Figure 4.3: Wire movement

The most important aspect of thermal modelling of the wire-sawing process is to determine the heat flux entering the work piece from the wire and the heat exiting from the new surface formed due to surface convection.

4.4.3.1 Heat Flux entering the work piece

Heat flux entering inside the ingot depends upon several factors including wire and slurry parameters. An analytical model has been developed by Bhagwat and Kao [4] to model this heat flux, Q as a function of power supplied to the wiresaw machine P ($\mathrm{W\,m^{-2}}$), area being machined A ($\mathrm{m^2}$) and a dimensionless quantity η representing the fraction of power that is transferred as compared to the amount that is actually being used for slicing,

$$Q = \frac{\eta P}{A} \tag{4.9}$$

The power P can be further expressed as,

$$P = Tv \tag{4.10}$$

where T (N) is the tension set in the wire during slicing, v ($\mathrm{m\,s^{-1}}$) is the velocity of the wire during sawing. The area being machined can be expressed as,

$$A = \pi RL \tag{4.11}$$

where R (m) is the radius of the groove formed during slicing, L (m) is the contact span. Contact span is the length of wire in contact with the ingot as shown in Figure 4.3. The dimensionless quantity η is a function of bow angle α that the wire makes with the horizontal axis because of bowing while slicing. The force exerted by the wire can be resolved into horizontal and vertical components. The vertical component of the tension is assumed to be responsible for the slicing and can be expressed as $T\sin(\alpha)$. As discussed in Sec. 2.4, the wire pressure while wire sawing is a function of contact span length L. Thus, taking these two factors into consideration, the dimensionless constant ϵ can be defined as

$$\eta = \sin(\alpha) \times L \tag{4.12}$$

η should also include a constant for the amount of heat dissipating in the slurry. Yamada et al [49] have estimated that 1/3 to 1/2 of the heat from the wire is taken away by the slurry. However, for this analysis, this loss of heat by slurry is ignored.

The flux entering also depends on the length of heat source l_s i.e., which is shown in Figure 4.3 as $\pi R/2$. During the finite element formulation of this process, however, the flux applied is multiplied with the length of the element l_e instead of l_s. There is an issue in this approach if l_e is greater than l_s as it will supply extra flux in every step. To balance this, a factor l_s/l_e is also multiplied to the supplied heat flux. The heat flux increases with cutting depth until the center is reached after which

it symmetrically decreases. The increase in flux with the depth is shown in Figure 4.4.

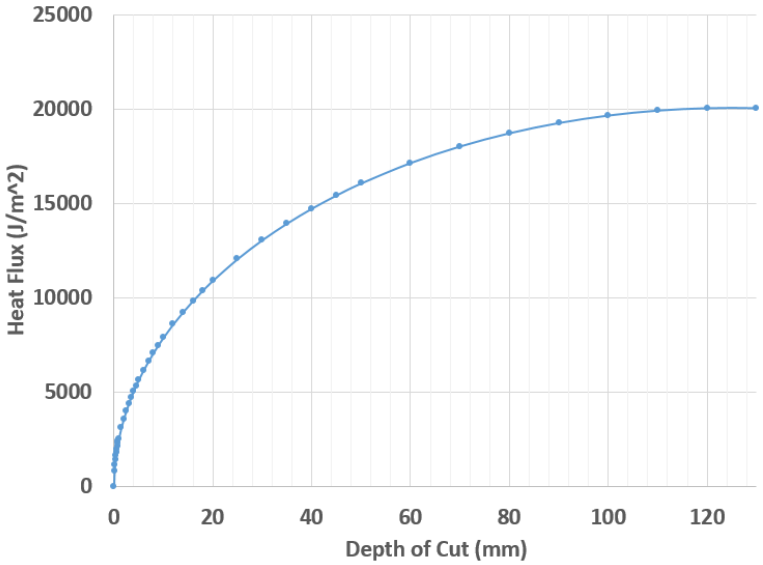

Figure 4.4: Heat flux with cutting depth

4.4.3.2 Heat flux leaving the workpiece

During wire sawing simulation, a new surface is created at each step of the model. All surfaces that are exposed to the air during slicing, including the newly formed surfaces, are to be applied with a natural convection boundary condition.

Si surface has a natural convection coefficient of $h = 5\ \mathrm{W\,m^{-2}\,K^{-1}}$ [4]. However, this value can not be used for the newly formed wafer surfaces. This is because the new formed surfaces are very close to each other and convection through their surface is affected by the combined movement of slurry, wire and abrasives particles. For this simulation, effective surface convection coefficient data is taken from Bhagavat and Kao [4], and shown in Figure 4.5. At the cutting position near the feed reference, the convection coefficient is $5\ \mathrm{W\,m^{-2}\,K^{-1}}$, while at the center of ingot it is $0.5\ \mathrm{W\,m^{-2}\,K^{-1}}$.

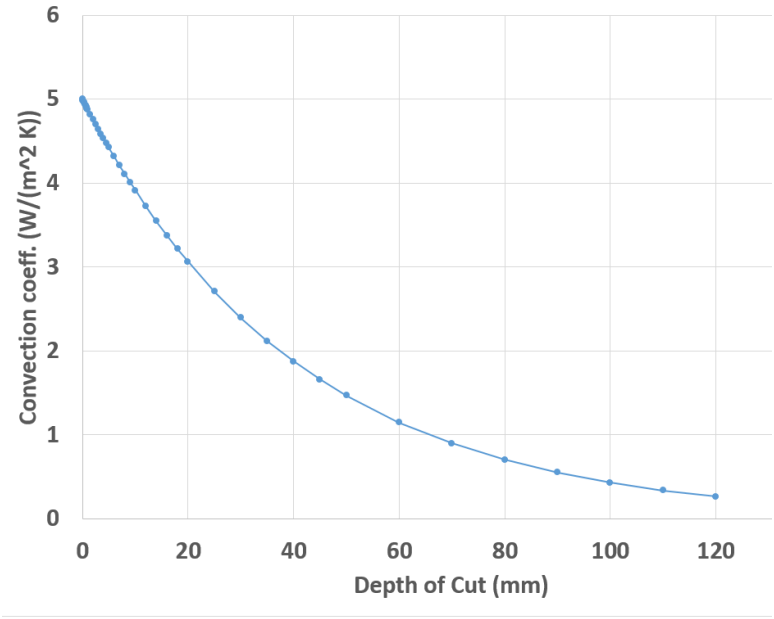

Figure 4.5: Heat flux with cutting depth

4.4.4 Wire Sawing: Displacement Model

Stress, strain and dislocation density results from the casting displacement model are required as the initial conditions for the wire sawing displacement model. This was done by mapping the results from the casting mesh onto the wire sawing mesh. Similar to the casting displacement model, temperature was taken from the wire sawing thermal model at each step in ABAQUS as a pre-existing temperature value. The mechanical boundary conditions supplied were pinning of nodes at the edge points where the wire leaves the work piece. This was done because the work piece is mounted on an ingot-holder at this end during the sawing process.

4.5 Relevant equations

In any physical process which involves the application of mechanical load, the overall strain in the system is the summation of strain contributions from several factors. In the current work, the total strain is assumed to be the sum of elastic, plastic, thermal

and dislocation creep strain given as,

$$\epsilon = e^{el} + e^{pl} + e^{thermal} + e^{creep} \tag{4.13}$$

In an isotropic medium, the rate of change of the elastic strain tensor $\dot{\epsilon}_s^{el}$ is given as,

$$\dot{\epsilon}_s^{el} = \frac{1+v}{E}\dot{\sigma}_s - \frac{v}{E}tr(\dot{\sigma}_s)I \tag{4.14}$$

where v and E are the Poisson's ratio and the elastic modulus. The rate of change of thermal strain is given as,

$$\dot{\epsilon}_s^{T} = \alpha'\dot{T}I$$

where α' is the coefficient of thermal expansion as discussed in the material property. In this simulation, it is assumed that the material deforms within the elastic limit and hence no plastic strain is considered,

$$\dot{\epsilon}_s^{p} = 0$$

The constitutive equation for creep strain is obtained by implementing the HAS dislocation growth equation. As discussed in the literature review, this equation connects the stress-dependent dislocation density with the creep strain rate. In a multiaxial form, the HAS equation can be written as,

$$\dot{\epsilon}_s^{creep} = \frac{1}{2}bk_0(\sigma_{eff})^P exp(-Q/k_bT)N_m\frac{1}{\sqrt{J_2}}\cdot S_{ij} \tag{4.15}$$

$$\dot{N}_m = Kk_0(\sigma_{eff})^{P+\lambda} exp(-Q/k_bT)N_m \tag{4.16}$$

$$J_2 = \frac{1}{2}S_{ij}S_{ij} \tag{4.17}$$

$$S_{ij} = \sigma_{ij} - \frac{1}{3}\sigma_{kk}\delta_{iij} \tag{4.18}$$

where b is the magnitude of the Burgers vector, σ_{eff} the effective shear stress, Q the Peierls potential, k_b the Boltzman constant, T the absolute temperature of the Si crystal, N_m the density of mobile dislocation at any time, S_{ij} the deviator component of stress, J_2 the second invariant of the stress deviator and k_0, K, P and λ the material parameters. The parameters used in the HAS model, except the Boltzman constant, are material specific.

The value for each of these parameters for Si is taken from Maroudas and Brown [27] and are given in Table 4.5.

Table 4.5: Value of parameters in HAS equation [27]

K ($\mathrm{m\,N^{-1}}$)	b (m)	k_0 ($\mathrm{m^{2+m}\,N^{-m}\,s^{-1}}$)	Q (eV)	P	λ	D ($\mathrm{m^{-1}\,N}$)
3.1×10^{-4}	3.8×10^{-10}	8.6×10^{-4}	2.2	1	1.1	4

It should be noted that in ABAQUS, during implementation of this constitutive creep equation, the strain is supplied as equivalent creep strain. Equivalent strain is obtained by replacing S_{ij} in Equation 4.15 with equivalent Von Mises stress given as,

$$\sigma_v = \sqrt{\frac{3}{2}S_{ij}S_{ij}} = \sqrt{3J_2} \tag{4.19}$$

and then solving for $\dot{\epsilon}_s^{creep}$. The effective stress σ_{eff} in Equation 4.15, which is the stress available to multiply and increase the dislocation density, is written as,

$$\sigma_{eff} = \begin{cases} \sqrt{J_2} - D\sqrt{N_m}, & \text{if } \sqrt{J_2} > D\sqrt{N_m} \\ 0, & \text{if } \sqrt{J_2} \leq D\sqrt{N_m} \end{cases} \tag{4.20}$$

where D is the strain hardening factor. σ_{eff} can be positive or 0 depending on the value of dislocation density and equivalent stress. If σ_{eff} is 0 then, as given by Equation 4.16, there is no change in the dislocation density. With an increase in

the dislocation density, the second term in Equation 4.20 increases, which leads to a decrease in σ_{eff} and, thus, the dislocation multiplication rate. This further means that the increase in the dislocation density will mostly be observed in the initial stages of deformation.

The stress relaxation is obtained through Hooke's law by substituting the value of elastic strain with the total, thermal, and creep strain shown as,

$$(\sigma) = [D^{el}](\epsilon^{el}) = [D^{el}](\epsilon - \epsilon^{thermal} - \epsilon^{creep}) \tag{4.21}$$

The stiffness matrix $[D^{el}]$ depends upon the Young's modulus and the Poisson's ratio, whose values are provided as material properties during the analysis.

The thermo-mechanical analysis using dislocation creep constitutive behaviour starts by assigning an initial dislocation density N_m^0 and initial temperature field. At each numerical increment in ABAQUS, the change in temperature is translated into thermal and creep strain and the convergence checks are done by ABAQUS. Upon convergence, the stress/strain and dislocation field are updated and the dislocation increment rate calculated and stored in order to calculate the creep strain in the next increment. The final dislocation density and the residual stress state is obtained upon the completion of the simulation.

4.6 ABAQUS Implementation

In this section, the development of models for directional solidification, wire sawing and mapping of results in ABAQUS is discussed.

4.6.1 Directional Solidification

The development of a model in ABAQUS simulating directional solidification was straight forward. The governing equations for different states were solved on the mesh along with the supplied boundary and initial conditions. These were discussed

in the previous sections.

4.6.2 Wire Sawing

The finite element model of wire sawing was developed to simulate the material removal due to wire movement along the cutting direction. The material removal process was discretized into several smaller steps, as shown in Figure 4.6. During each ABAQUS step, one row of elements were removed from the mesh to simulate the thin layer of material removed and the heat transfer and the stress-strain equations were solved accordingly. Each step in the ABAQUS input file had 3 attributes that were dependent on the location of the cut. First, the magnitude of the heat flux entering. Second, the magnitude of heat leaving. And third, the time size of that step.

The magnitude of the heat flux entering in the work piece from the wire and heat leaving due to convection from the new surface is applied as a thermal load and a film boundary condition, respectively, with the values as per discussed in Section 4.4.3. The time step size was calculated based on the contact length between the wire and the ingot at the current step. This is discussed in as follow.

The overall model was developed to simulate for a 400 minute wire sawing process since this is the industrial time scale of this process [4]. Time size $\triangle t^i$ for all the steps $i = 1, 2, ..$ were not equal. The time size of each step is dependent on the material removal rate which is, as discussed in the literature review [31], is given as v_s,

$$v_s = \frac{m \ \ V_0}{A_s \ \triangle t} \tag{4.22}$$

where m is the indentation events per unit contact area A_s in time $\triangle t$ and V_0 is the material removed per indentation event. Based on indentation and fracture mechanics, V_0 has been found to be a function of normal force F_N acting on the work piece as:

$$V_0 = F_N^{2.2} \tag{4.23}$$

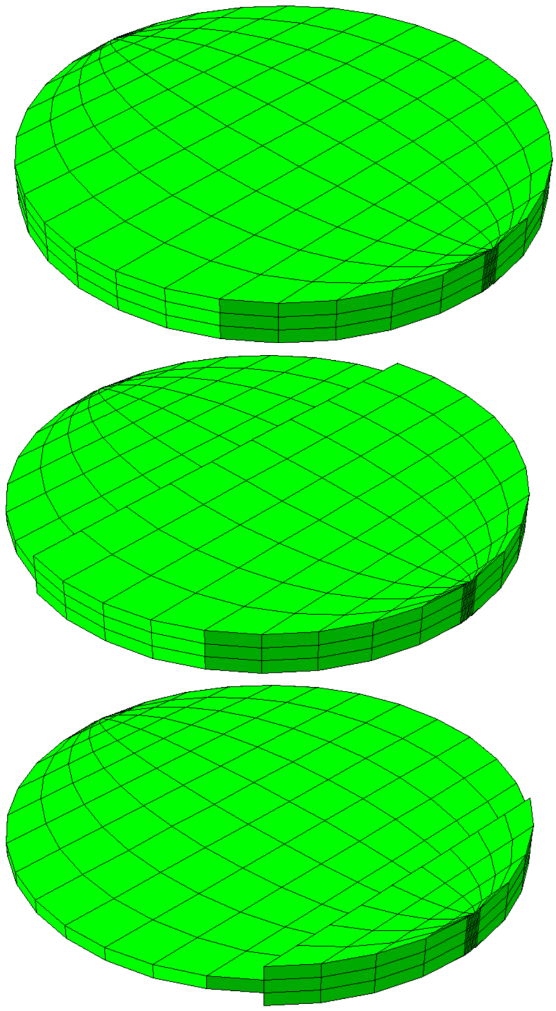

Figure 4.6: Figure to display the mesh removal during cutting to simulate the material removal process

It is self-evident that A_s, at any given point in cutting, is directly proportional to the contact length between the wire and the work piece. Based on Equation 4.22, it can be said that the material removal rate v_s is, therefore, also a function of the contact length,

$$v_s = \frac{1}{\omega L_x} \tag{4.24}$$

where ω is a proportionality constant. It is assumed that the value of ω is dependent on the slurry, the abrasives particles' shape and size and independent of the contact length. In this work, those factors are not studied, and so a constant value of ω is taken for all contact lengths. This model was developed for a cylindrical work piece geometry. Time steps size for each steps were calculated beforehand as a function of

depth of cut and then supplied in ABAQUS as respective step time size. The time step size $\triangle t_x^i$ required to remove a strip of material $\triangle x^i$ at depth of cut x at the ith step can be written as,

$$\triangle t_x^i = \frac{\triangle x^i}{v_s^i}$$

$$\triangle t_x^i = \omega L_x^i \triangle x^i \tag{4.25}$$

$$L_x = 2\sqrt{R^2 - (R-x)^2)}$$

where R is the radius of the workpiece. In order to supply the value of time step $\triangle t_x^i$, the value of ω was required. This value of ω was approximated based on the total time the wire sawing process took. Total time during wire sawing was written as the integration of all the $\triangle t_x^i$,

$$\int_0^T dt = 2\int_{-R}^{R} \omega\sqrt{(R^2 - (R-x)^2)}dx \tag{4.26}$$

Since ω is constant with x, it can be written as,

$$T = 2\omega \int_{-R}^{R} \sqrt{(R^2 - (R-X)^2)}dx = 4\omega R \tag{4.27}$$

$$\omega = 400/4R = 400/(4 * 125) = 0.8$$

This value of ω was used in Equation 4.25 while discretizing the time steps for the thermal and stress/strain finite element model of the wire sawing process.

The ABAQUS input file for the thermal and the stress wire sawing model was developed using python. The whole input file was split into various modules such as mesh geometry, material property, steps to simplify its creation. In the mesh geometry construction module, the row wise collection of elements were assigned element group, surface group and node group names. This was done so that in the steps con-

struction module, these surface/node/element names can be called and assigned the respective thermal load, boundary conditions and element deletion. The step module created steps in the input file by iterating through python loops. In each loop, one layer of wafer was removed. This was done by applying model change command in ABAQUS on the element row that was to be removed in that step. Upon removal of element layer, new surface was formed, as shown in Figure 4.7. Surface flux was activated on the new surface. Apart from element removal and surface flux activation, thermal load was also applied on the new surface formed. The magnitude of surface flux, thermal load and time step in each step loop was applied based on the loop number. Each loop number signified a particular depth of cut. Similar strategy was used for the stress input file generation too.

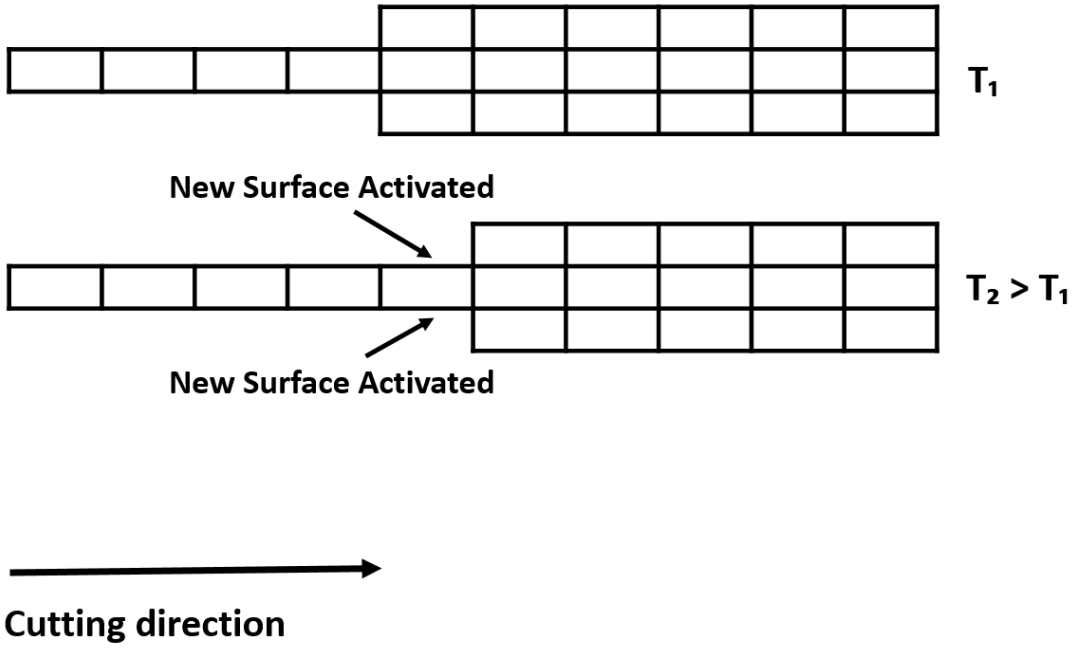

Figure 4.7: Construction of step for the thermal input file.

4.6.3 Mapping

The wire sawing simulations required results from the casting simulations to be mapped as initial conditions. The casting simulations were performed on a 2D axisymmetric mesh to save computational time and the wire sawing simulations were

performed on a non-symmetric 3D mesh. Therefore, mapping was a challenging task.

The mapping of stress fields was a 3 step procedure, as shown in Figure 4.8. First, the rotation of 2D axisymmetric result into a 3D result. Second, mapping this 3D result on the wire sawing mesh to occupy the same volume. Third, deactivating the elements of the mesh where the wire sawing simulation was not being done.

During the third step, while deactivating the parts of the mesh, it was important to prevent stress release. This challenge was overcome by applying a mechanical pinning boundary condition. The mapping of results was only done at three locations. The detail of this will be further discussed in the next chapter.

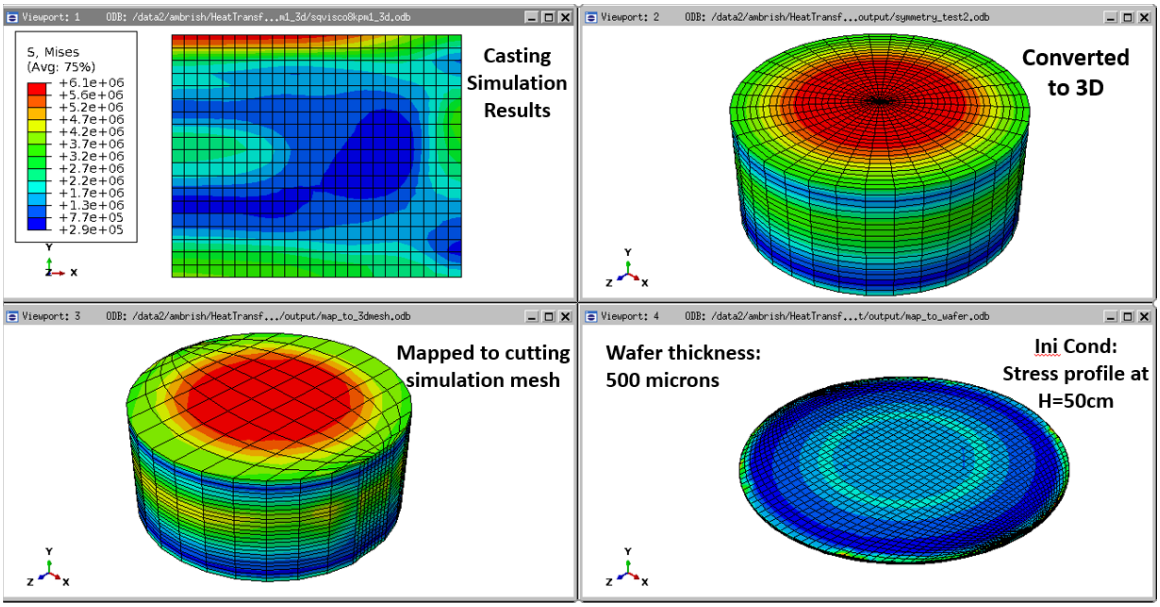

Figure 4.8: Figure to display the transfer and the mapping of the casting results from the axisymmteric mesh on the wire sawing simulation mesh.

Chapter 5

Results and Discussions

In this chapter, the results of our thermo-mechanical simulation of mc-Si solidification and wire sawing processes are presented and discussed. For both of these processes, the thermal simulation provided the temperature variation and the stress/strain simulation provided the residual stresses and strains and the final dislocation state. The spatial and temporal variation of these results will be discussed to analyse their dependence on the processing conditions.

5.1 Casting: Thermal Simulation

As discussed in Section 4.2, the thermal simulation for casting was carried out by cooling the bottom surface of the ingot at 2, 5 and 8 K/Min. This was implemented by applying a Dirichlet boundary condition on the bottom surface. The results of these simulations are shown in Figure 5.2. Before moving on to the results, the relevant point of interest for which the results are presented are shown in Figure 5.1. Point A is located at the bottom radial center of the ingot, point B is located at a height of 1/4th of ingot height above point A, point C is located at 1/2 of the ingot height above point A and point D is located at the center of the top most surface of the ingot.

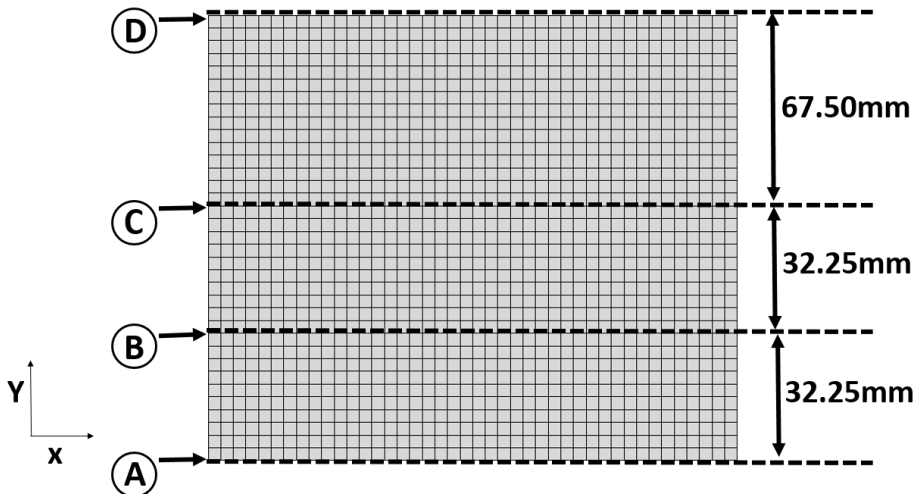

Figure 5.1: Casting mesh and the relevant point of interests

Thermal gradients during casting lead to thermal strains, therefore, a temperature gradient graph between the bottom and the top part of the ingot can provide a qualitative insight into the effect of cooling conditions on the final ingot stress/strain and dislocation density. As seen in Figure 5.2, the thermal gradient between point A and C and point A and D is high at the melting point due to the release of the latent heat of fusion. In the case of 8K/min cooling, this gradient is approximately double as compared to the 2K/min cooling case. With further cooling, this gradient gradually decreases and plateaus until it finally vanishes at the end of the process. The magnitude of this plateau is dependent on cooling rate and is maximum for 8K/Min.

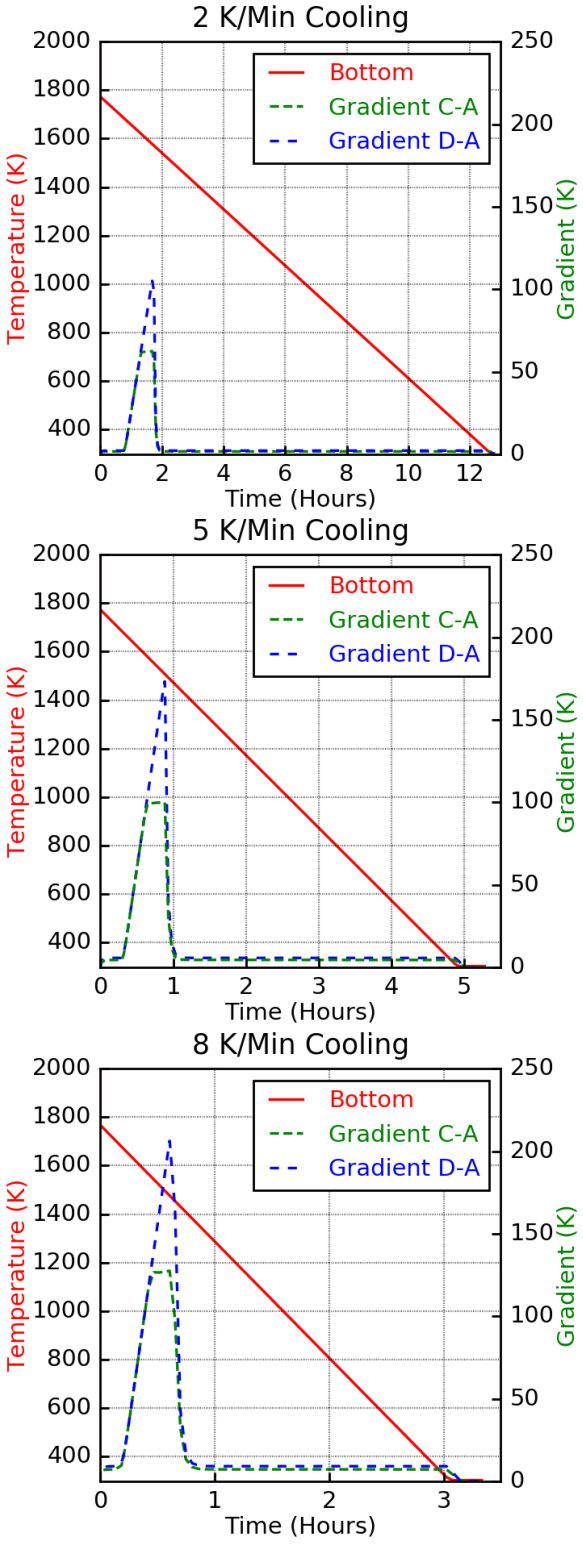

Figure 5.2: Variation in temperature and temperature gradient between the top-bottom and the middle-bottom with time

Another interesting thing to observe here is that the spike in temperature gradient exists for a longer time period in case of 2K/min cooling condition. As discussed

in Chapter 2, the creep strain rate in the HAS model is a function of the thermal strain and specifically is an exponential with a temperature term. This means that the accumulated creep strain is dependent both on the magnitude of thermal strains developed and the time duration for which the ingot was exposed to high temperature. For the case of 2K/min cooling, even though the thermal gradient (and thermal strain) is low, the time for which this strain is applied is long compared to the 5 and 8 K/min cooling. This may therefore influence the strain dependent dislocation density in the ingot and render slow cooling ineffective in lowering down the dislocation density.

5.2 Casting: Stress Simulation

As discussed in Section 4.2, the stress model for casting was developed to simulate the stress/strain state during solidification using the HAS model, which incorporates the dislocation-creep behaviour. The predicted temperature-time results from the thermal model were used as temperature inputs for this model.

The change in dislocation density with temperature and time is displayed in Figure 5.3. These graphs are for the bottom and the top of the ingot (shown as Point A and D respectively in Figure 5.1). For all the 3 cooling cases, the increase in dislocation density occurs just below the melting point, which can be attributed to the strains developed due to the mismatch in the temperatures between A and D. This mismatch is evident from the hold in the temperature curve from the top part. The rise in the dislocation density in the top and the bottom part is not the same and more for the bottom case. This may be due to the assumption of the contact/pinned boundary conditions applied at center bottom of the ingot. With an increase in the cooling rate, the final dislocation density as well as the difference between the dislocation density in the top and the bottom part increases.

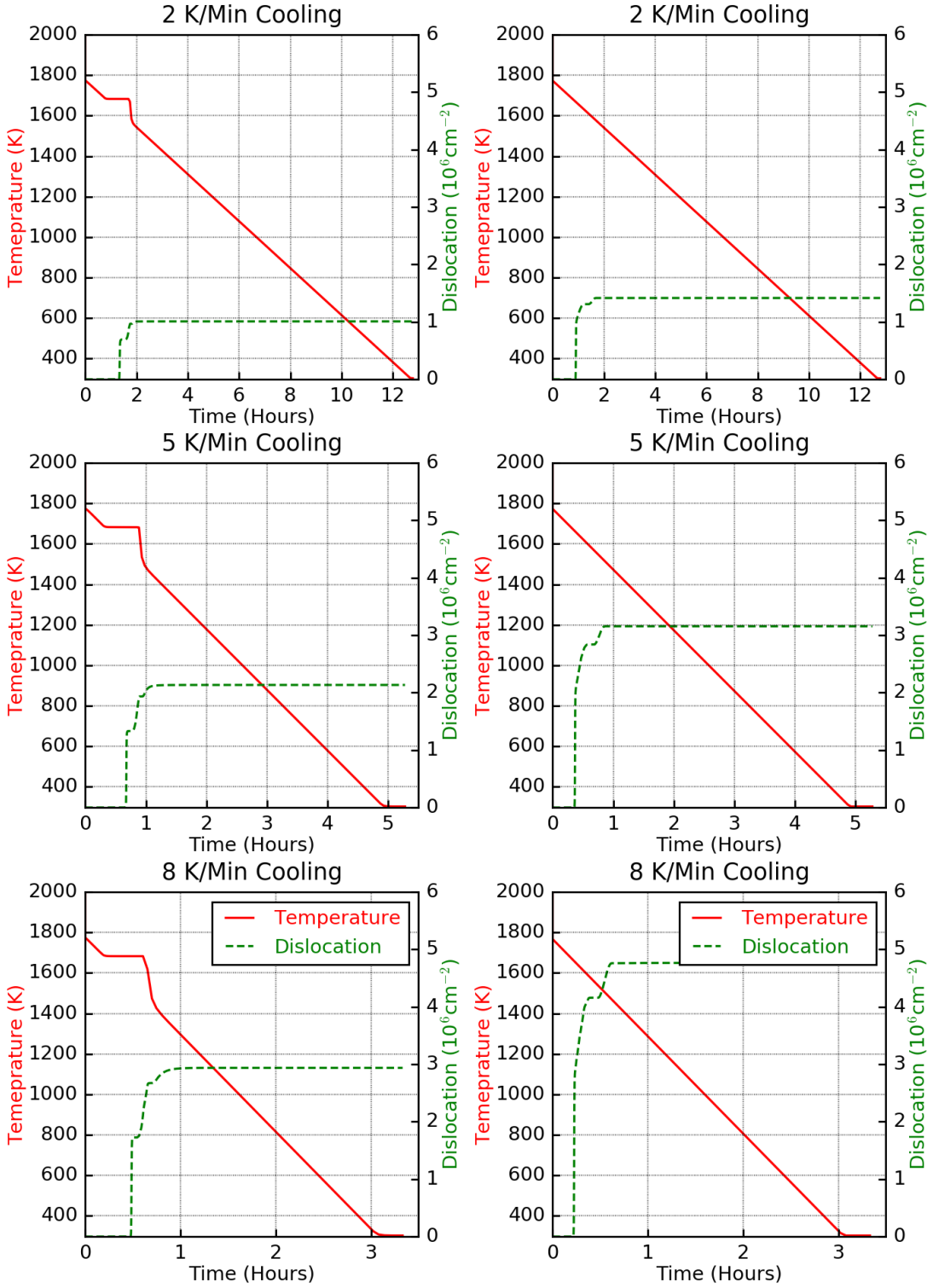

Figure 5.3: Comparison of temperature and dislocation density with time for all the three cooling conditions for top (left) and bottom (right) of the ingot.

The variation in dislocation density with equivalent stress are shown in Figure 5.4. The stress curve has four phase. First, the initial spikes. Second, the decrease in spikes. Third, the gradual increase. And fourth, the final plateau. The initial spikes in the stress occurs due to the large thermal strains from large thermal gradient during the liquid to solid transition phase. The decrease in spikes occurs due to inelastic yielding, discussed in the next paragraph. The gradual increase in the stress occurs due to the increase in Young's Modulus with the decrease in the temperature. And finally, once the temperature across the ingot reaches final temperature, the stress reaches its final value.

The dislocation density starts increasing when the equivalent stress spikes. With the increase in dislocation density, the equivalent stress falls, which is expected due to stress relaxation manifested in dislocation-creep inelasticity. The final dislocation density is highest at 8 K/min and lowest at 2 K/Min. Comparing this figure with Figure 5.2, it can be seen that the spikes in equivalent stress exists until the gradient between the bottom and the top part of the ingot reduces to a small value. These spikes are proportional to the magnitude of the gradient itself. This is why in the case of 8K/min cooling, the equivalent stress rises to a higher level leading to a higher dislocation density.

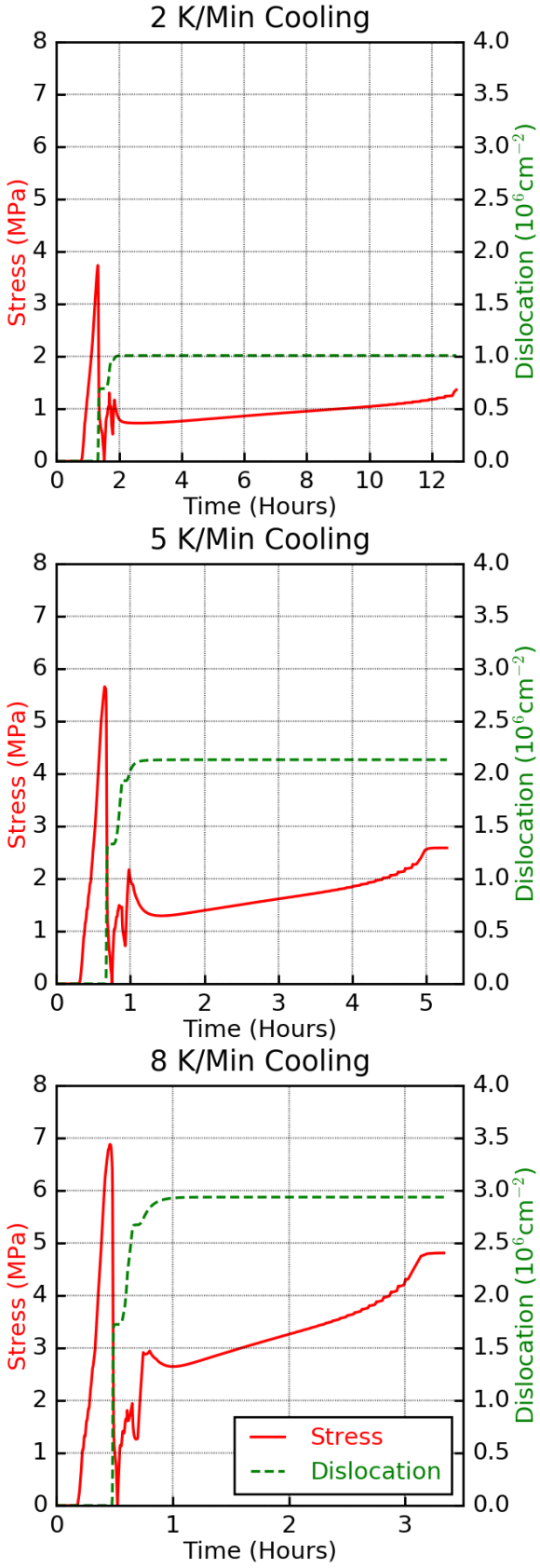

Figure 5.4: Comparison of equivalent stress and dislocation density with time for all the three cooling conditions.

Based on Figure 5.4, it can also be seen that the residual stress and the final dislocation density both increase in response to increases in the cooling rate from 2K/min to 8K/Min. It is a well known fact that in absence of any inelastic/plastic deformation during cooling, there is no residual stress. However, in this case, due to dislocation-creep, which is an inelastic form of stress relaxation, residual stress is developed whose magnitude is proportional to the level of creep deformation itself. The level of creep relaxation is manifested by the final dislocation density. Therefore, final dislocation density and the residual stress both increase alongside with increase in cooling rates.

Figure 5.4 is consistent with the HAS model in that it shows that the dislocation density rises when the equivalent stress reaches a high level. This is because in the HAS equation, the driving force for dislocation growth is the 'effective' stress instead of the actual stress, as discussed in Equation 4.20,

$$\sigma_{eff} = \begin{cases} \sqrt{J_2} - D\sqrt{N_m}, & \text{if } \sqrt{J_2} > D\sqrt{N_m} \\ 0, & \text{if } \sqrt{J_2} \leq D\sqrt{N_m} \end{cases} \tag{5.1}$$

This effective stress is a function of both the equivalent stress and the current dislocation density. Due to the presence on an initial dislocation density, the equivalent stress has to first reach a critical level before it can start the multiplication of dislocation. As shown in Figure 5.5, the dislocation density only increases when the effective stress is positive.

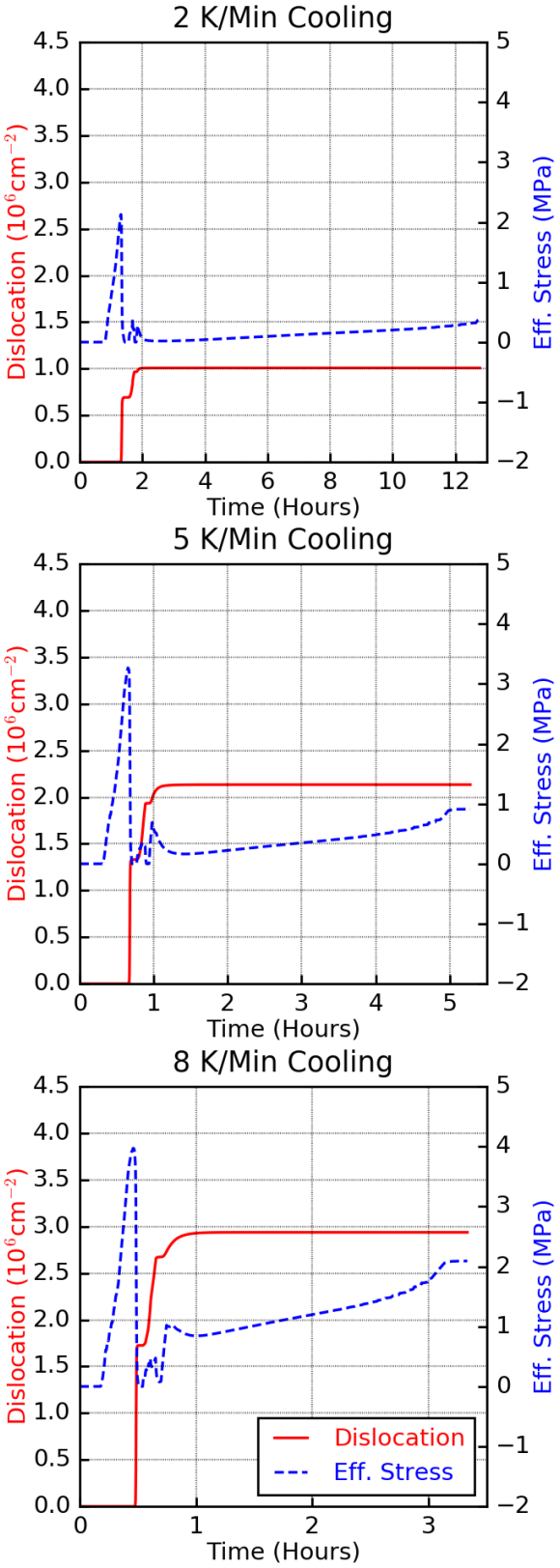

Figure 5.5: Comparison of effective stress and dislocation density with time for all the three cooling conditions. The dislocation density increasing only when the effective stress is positive.

Another point to observe in Figure 5.4 is the fact that the dislocation curves, very strongly, plateaus after the initial phase of cooling. It should be noted that in this plateau region, the high levels of stress do not lead to any change in the dislocation density curve. This is because of two reasons. First, as per the HAS equation, the back stress ($D\sqrt{N_m}$, as discussed in Equation 5.1) against dislocation growth increases with an increase in the dislocation density. Physically, it means that with increasing dislocation density, it becomes more difficult to move and grow dislocations as they act as barrier preventing further multiplication and growth. Back stress and dislocation density is shown in Figure 5.6. The second reason for this plateau is the fact that HAS equation has an Arrhenius type dependence on temperature. Due to this, the dislocation growth is extremely small at lower temperature. Comparing Figure 5.4 and 5.3, it can be seen that below 1200K there is no change in the dislocation density in all the cooling cases and hence the observation of a plateau.

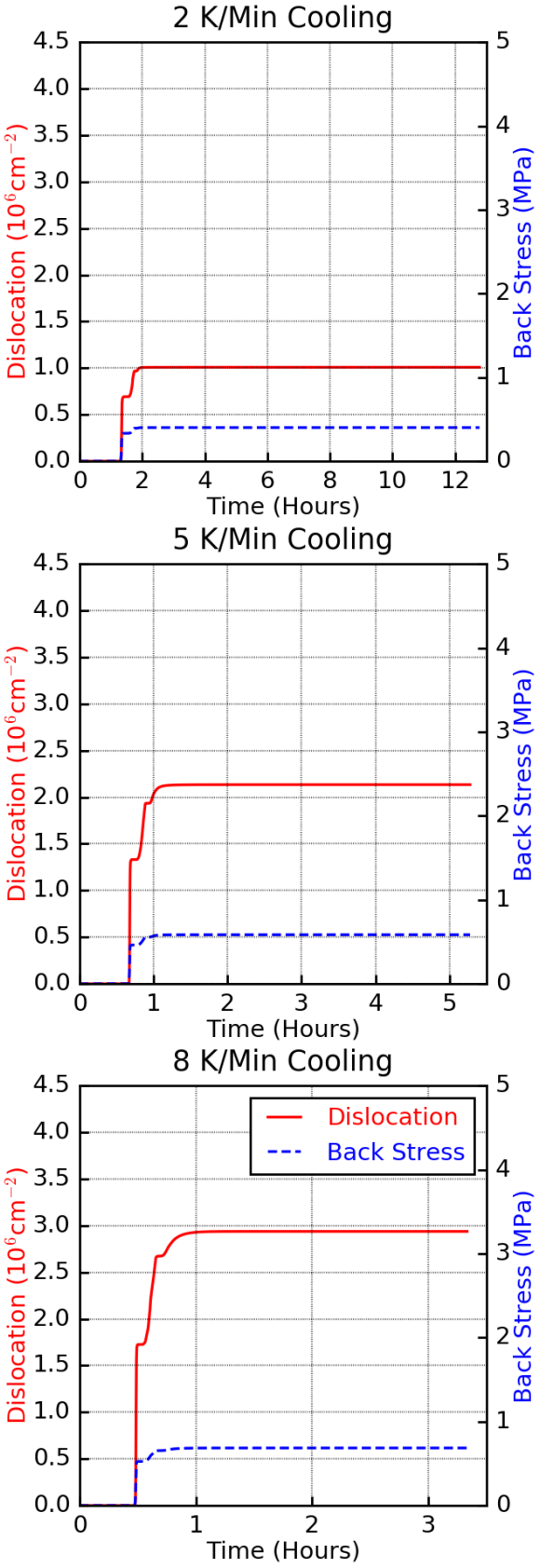

Figure 5.6: Comparison of back stress and dislocation density with time for all the three cooling conditions. Back stress increases with the increase in dislocation density

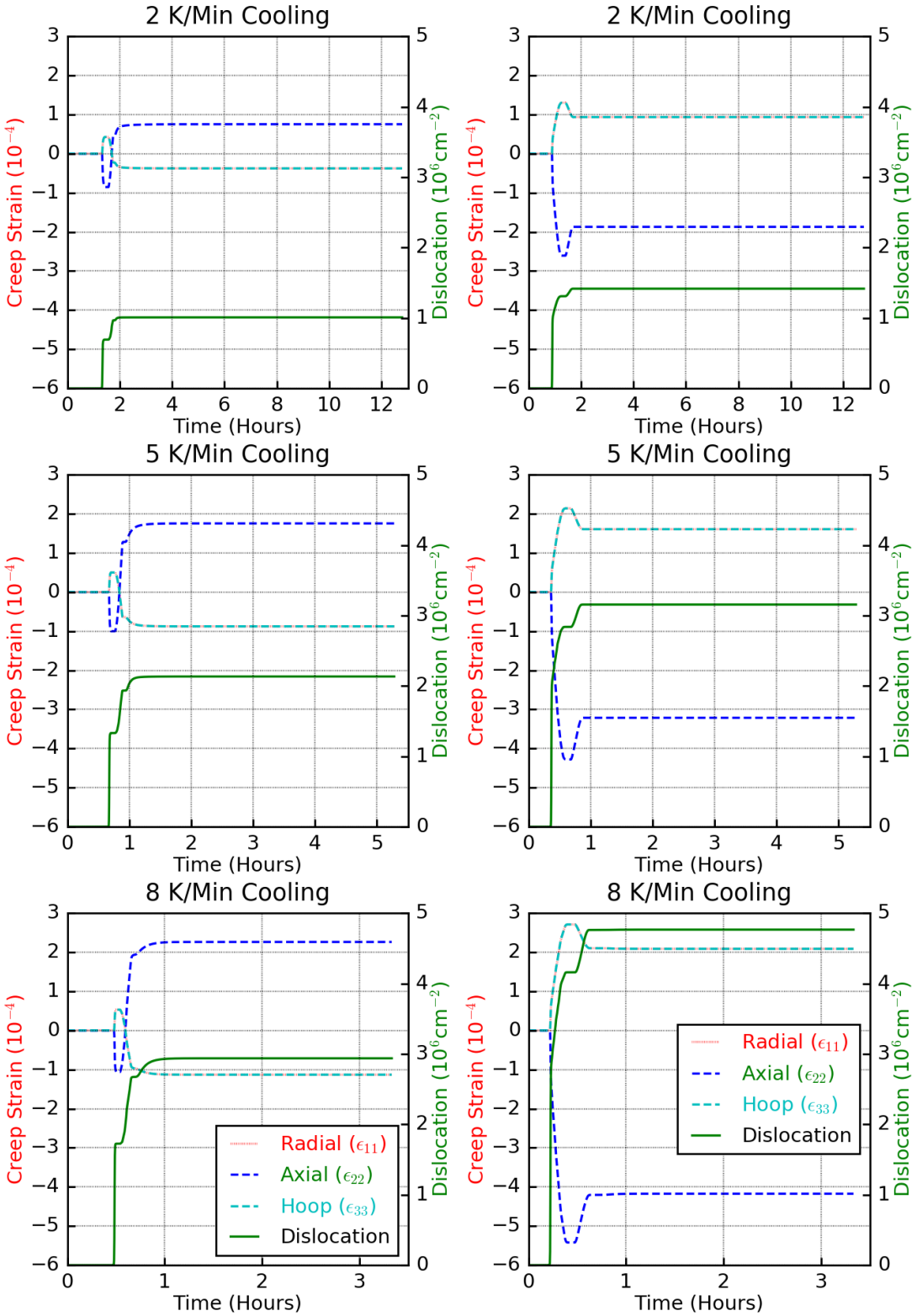

Figure 5.7: Comparison of radial (ϵ_{11}), axial (ϵ_{22}) and hoop (ϵ_{33}) strain with dislocation density and time for all the three cooling condition for top (left) and bottom (right) of the ingot.

It is a well known fact that during cooling, the outer region of a casting experiences tensile strain (+) resulting from its inability to undergo thermal contraction. This tensile strain leads to "expansion" through inelastic/plastic deformation. Upon further cooling, the outer region goes into a compressive strain (-) due to the contraction of the rest of ingot. The current simulation also presents a similar change in strain. The changes in the radial, hoop and axial creep strains with time is plotted in Figure 5.7 as a function of the growth of dislocation for the top and the bottom of the ingot. The radial and hoop strain increase at first, indicating compressive strain in radial and hoop direction and then a decrease indicating tension. The final state of radial, hoop and axial creep strain is different for the top and the bottom part. The top part of the ingot undergoes compression in the radial and the hoop direction and tension in the axial direction. The bottom part is in the exact opposite state of the top part.

Transition of stress state from tensile to compressive passes through a state of null stress. As per the HAS model, the dislocation growth should not occur at null stress. This (as expected) can be seen in the dislocation growth curve as it flattens at times where the creep strain curve changes sign. Interestingly, Franke *et al* [12] have also observed the presence of steps in the dislocation rise curve from their simulation.

To examine the variation in residual stress, contour maps of all the final elastic stress components are plotted in Figure 5.8. The part of the ingot near the central/symmetry axis is in compression at the top and bottom part and tension at the center in the radial and hoop direction. Away from the central/symmetry axis towards the edge, the ingot is in tension in the radial direction and in compression in the axial and hoop direction. By and large the contour follows a common pattern, edges in same stress state and center in the opposite state with absence of any transition regions (with zero stress) in between. The magnitude and severity of these stress variations increase with the cooling rates. This contour also shows that the final state of stress/strain in radial and hoop direction is independent of the ingot height. The model captures the initial transient phase followed by the final steady state where the

stress/strain in the bulk has a low spatial variation and becomes independent of the ingot height. This basically means that for a given ingot height, the bulk is mostly homogeneous in terms of residual stresses and strains. However, the magnitude of this homogeneous residual stress is, of course, dependent on the total ingot height.

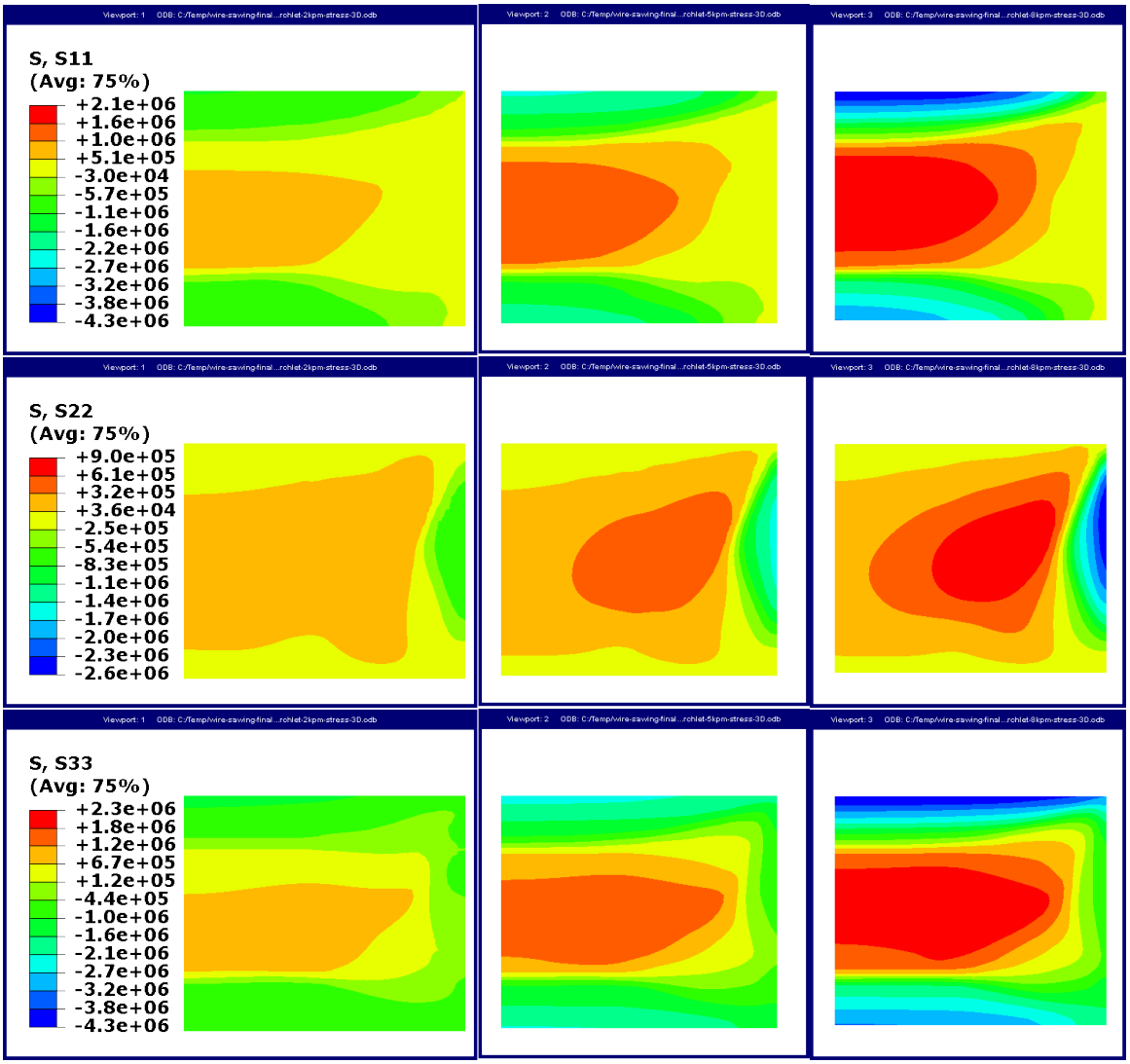

Figure 5.8: Final stress contour: Radial (S11), Axial (S22), Hoop (S33) for (Left to right) 2K/Min, 5K/min and 8K/Min

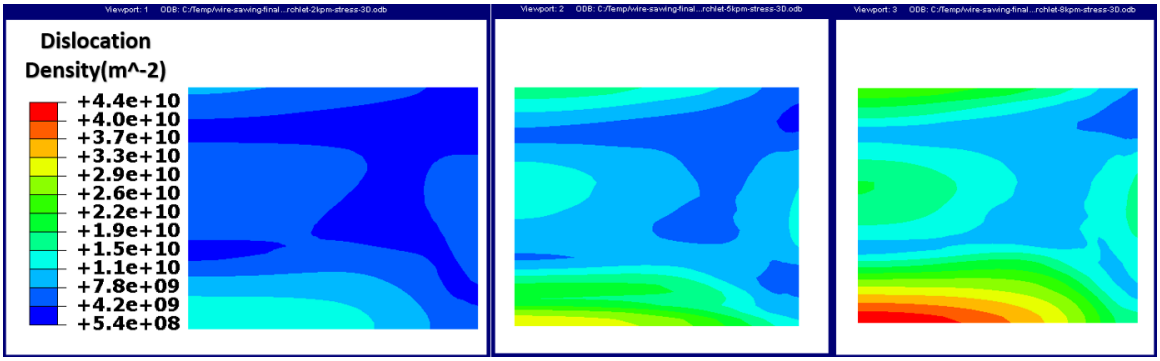

Figure 5.9: Final dislocation density (m^{-2}): (Left to right) 2K/Min, 5K/min and 8K/Min

The final dislocation density for all the cooling cases is plotted as a contour plot in Figure 5.9. The simulated dislocation density are in agreement with the literature [17] within two orders of magnitude, as shown in figure below.

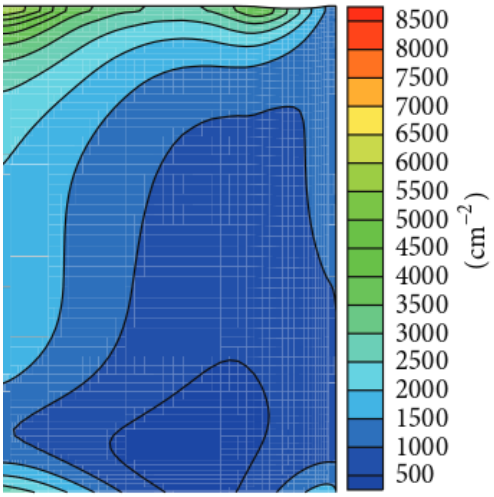

Figure 5.10: Dislocation density in half of directionally solidified mc-Si ingot cooled at 5 K/Min [17]

The overall magnitude and the spatial variation of dislocations is higher in case of 8K/min cooling as compared to 5K/min and 2K/min cases. This contour pattern is similar to the residual stress contour patterns from Figure 5.8. Higher creep deformation leads to higher dislocation density and it also leads to more stress relaxation. This is why the similarity in pattern is exhibited. The overall creep deformation is shown in Figure 5.11. As seen, the outer region have undergone a higher creep deformation. As seen, the outer region have undergone a higher creep deformation. The creep strain is

maximum for 8K/Min cooling due to the higher thermal strains. This creep doesn't covers the steady state regime creep. Alternatively, if the steady state creep equation was used instead of transient creep, then the creep strain would have been less. Any creep equation can have two component, one the steady state part (which makes the creep strain rate time independent) and second, the dislocation part (which makes the creep strain rate time dependent). Removing the dislocation part (to make it a steady state creep), the creep is bound to be low since the creep strain rate in Si steady state is much lower compared to that in transient case (as was shown in the Si creep curve).

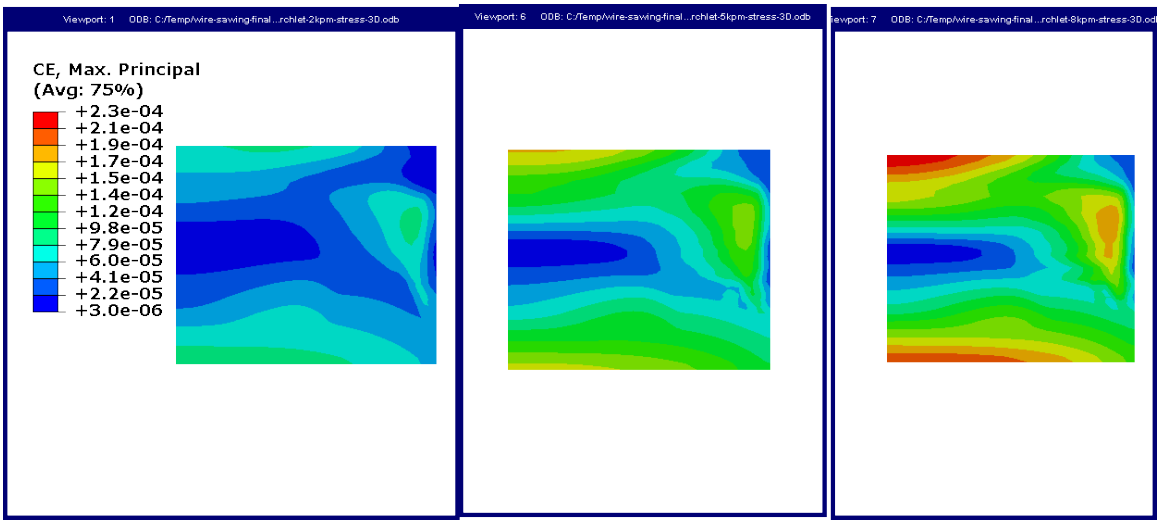

Figure 5.11: Final creep strain: (Left to right) 2K/Min, 5K/min and 8K/Min

5.3 Results transfer and mapping

As discussed in Section 4.7, the axisymmetric 2D results from the casting simulation were converted into 3D and then mapped onto the wire sawing simulation mesh. This mapping was done at only three locations, as shown in Figure 5.12. The mapped mesh had three element layer stacked together, the top and bottom of which were removed to simulate the cutting process. This is shown in Figure 5.13. The result fields being mapped were the elastic stress/strain and the dislocation density. This was done to understand the affect of initial residual stress in the work-piece on the residual stress, warpage and dislocation density in the wafers after wire sawing. Furthermore, the objective was also to understand if a wafer cut from different locations had different

levels of warpage and dislocation density.

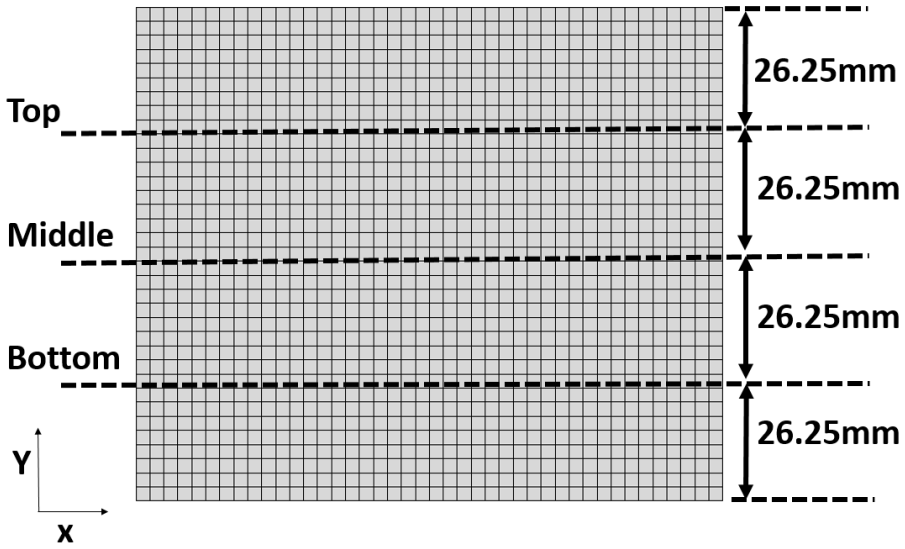

Figure 5.12: Figure to show the locations where the wire sawing simulation was done. Results from these three locations were mapped on the wire sawing simulation mesh.

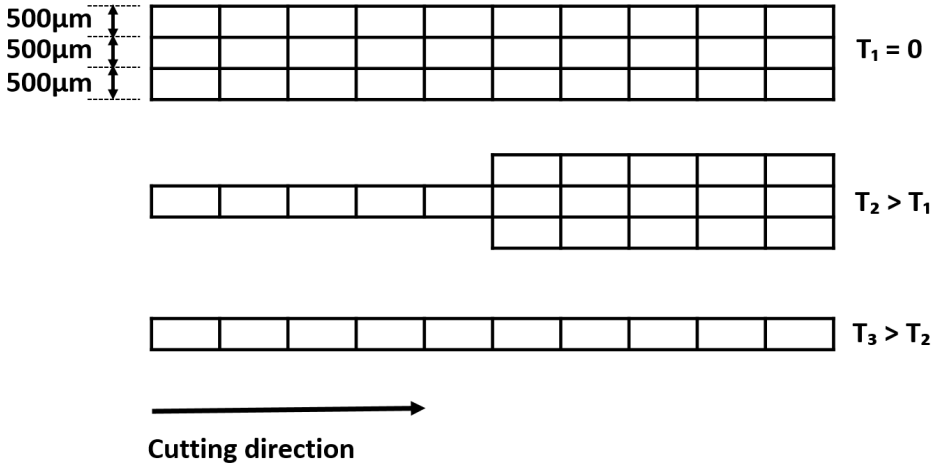

Figure 5.13: Figure showing the side view of the wire sawing mesh. The mesh has three element layers each 500 μm. The cutting process is removal of top and bottom layers using model change in Abaqus.

The mapped stress 'S-xx','S-zz' and the dislocation density for 8K/min cooling conditions are shown in Figure 5.14 and 5.15 respectively. Comparing these with Figures 5.8 and 5.9, it can be seen that the results were mapped closely. The slight difference in the mapping is due to the dissimilarity between the casting and the cutting mesh. Mapping in ABAQUS is done by extrapolating the variables. The wire sawing mesh has oval contours. This may lead to uneven extrapolation, which may be the reason for oval shaped contours after mapping. Furthermore, while mapping,

the radial stress is resolved into 'x' and 'z' components to calculate 'S-xx','S-zz'. Due to the dissimilarity between the meshing, there is an orientation difference during extrapolation.

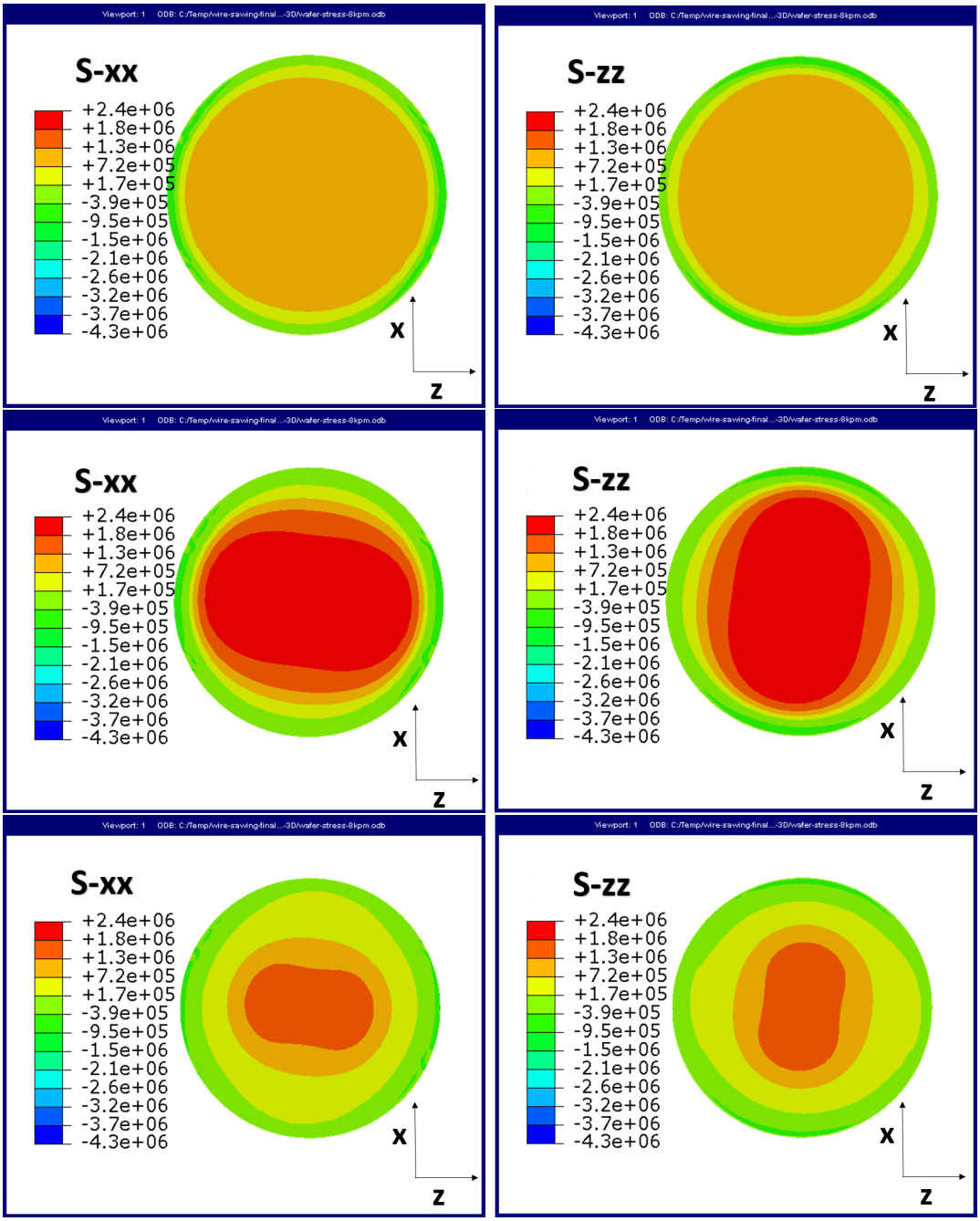

Figure 5.14: Mapped stress components S-xx and S-zz from top, mid, bottom sections (shown from top to bottom) for 8K/min cooled ingot.

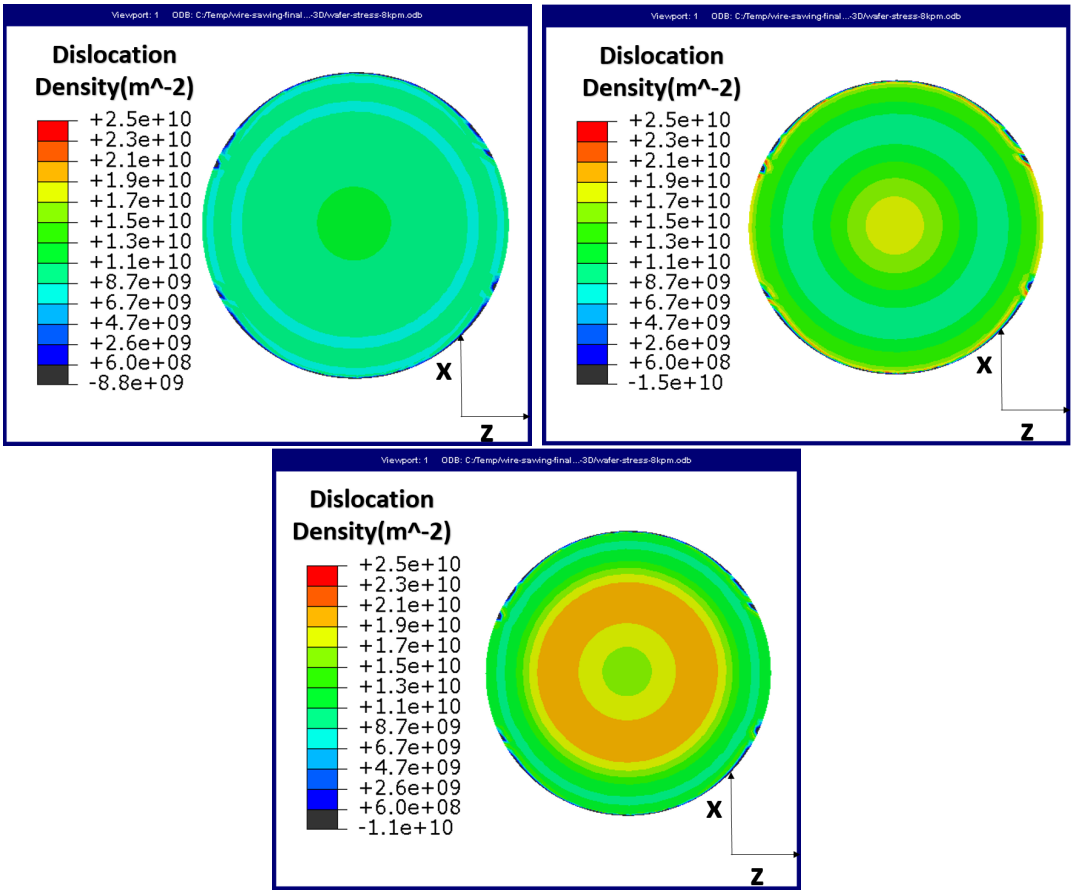

Figure 5.15: Mapped dislocation density from top, mid, bottom sections (shown from top to bottom) for 8K/min cooled ingot.

5.4 Wire sawing: Thermal simulation

The thermal simulation of the wire sawing was carried out using the heat flux and the material removal equations discussed in Section 4.6. It was also assumed that the temperature in the work piece during the sawing did not vary along its axis. Under this assumption, the thermal simulation domain was reduced to a small section instead of the complete ingot.

The evolution of temperature with time at various locations on the thermal simulation domain are shown in Figure 5.17. The mesh domain and points of interest are shown in Figure 5.16. Temperature rise during the wire sawing process is different at different locations. The peak levels of heating increase along the direction of cutting. The height of these peaks are 50-60 °C above the starting temperature

and is in close agreement with the literature on temperature rise during wire sawing [2, 4]. The maximum temperature gradient between the points at wire entry and wire exit is approximately around 15 °C and is observed during the middle of the sawing operation. This is shown in Figure 5.18.

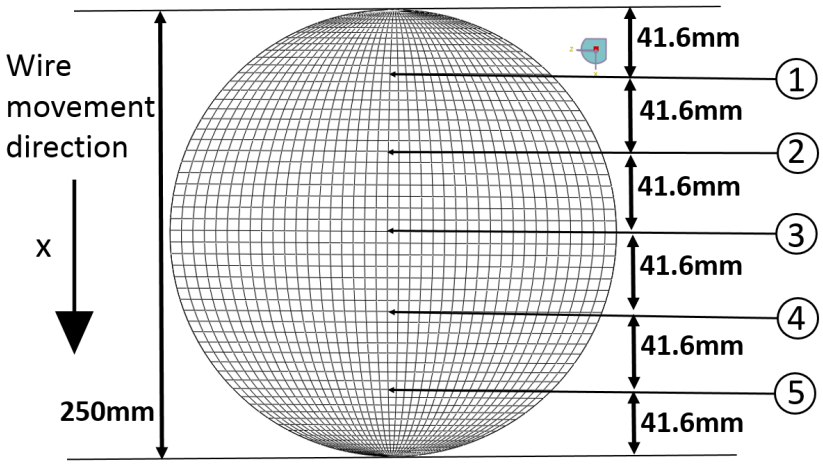

Figure 5.16: Wire sawing mesh and the relevant points of interest. These points are picked from the central axis of the wafer and are equally distributed along the wire sawing direction.

The peaks of the heating curves were expected to be at the center since the heat flux entering the work-piece is maximum at the center due to maximum contact length with the wire, as explained in Figure 4.4. This is combined with the fact that the heat flux exiting the work-piece through surface convection is minimum at the center as discussed in Figure 4.5. Due to these factors, the temperature rise is observed to be maximum during the middle of the sawing operation.

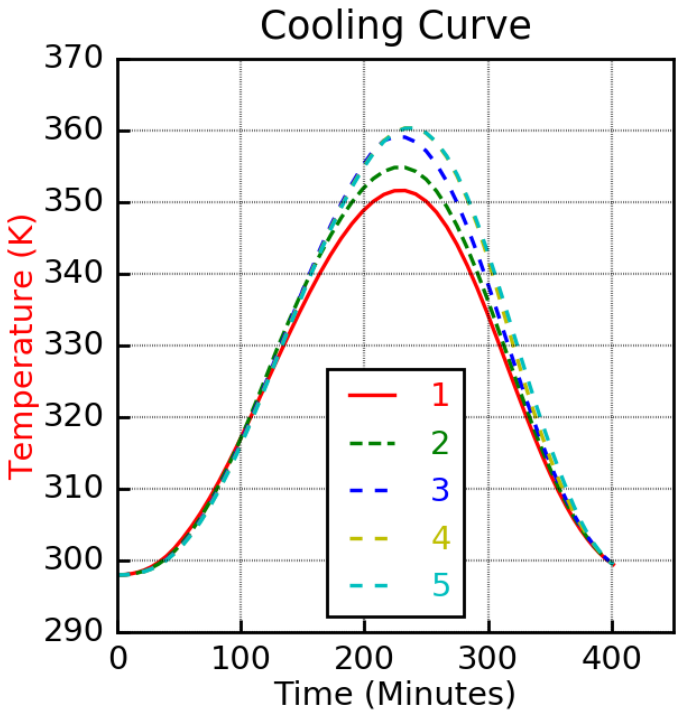

Figure 5.17: Temperature with time curve during wire sawing to shown temperature rise at points along the direction of cutting.

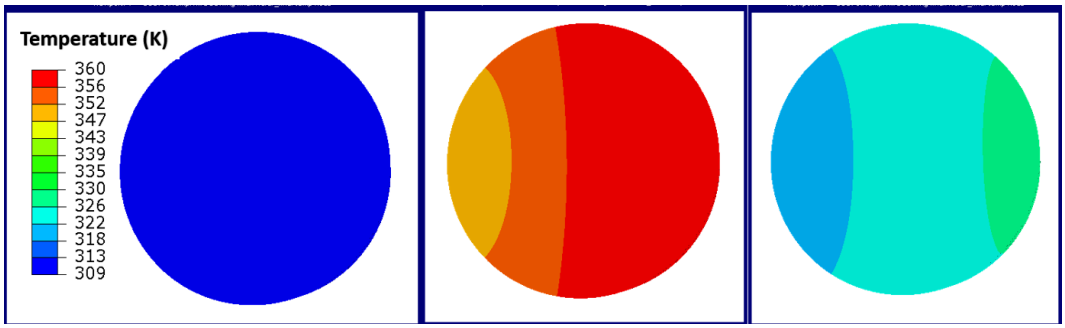

Figure 5.18: Contour plot of temperature at 25%, 50% and 75% of sawing completion (left to right).

5.5 Wire sawing: stress simulation

The warpage in wafers can occur due to inelastic deformation and/or stress relaxation during the process of cutting. This is explained as following:

- The inelastic deformation can occur due to temperature rise and thermal strain, resulting in a change in the shape of the wafer, thereby leading to warpage.
- The movement of wire leads to formation of a new surface which is free to bend.

This new surface may have an in-plane stress gradient (xz plane in this case) which is inherently present due to work piece initial residual stress. In order to establish a force equilibrium during cutting, the surface bends, leading to wafer warpage.

In order to understand the inelastic deformation during the cutting process due to temperature rise, the wire sawing stress simulation was performed using the temperature data obtained from the thermal simulation applied as a boundary condition. Furthermore, to predict *only* the effects of the temperature rise during sawing on warpage, the simulation was done without any initial residual stress. The predicted variation in the dislocation density with time from this simulation is plotted in Figure 5.19. The plots in the figure are shown for points 1, 2, 3 and 4, as discussed in Figure 5.16, lying in the mid plane (z=0) of the wafer along the cutting direction. It can be seen that the dislocation density remains constant, implying no inelastic deformation occurring in the wafers during the sawing process under the applied constitutive behaviour. This absence of inelastic deformation is because of two reasons, First, the equivalent stress levels are low during the process (due to a low thermal gradient as shown in Figure 5.18) as showed in the left of Figure 5.19, Second, due to the relatively small exponential factor of HAS model at low temperature. In the HAS model, due to an Arrhenius type relation of dislocation-creep strain rate with temperature, at lower temperatures a very high value of effective stress is required for dislocation multiplication and movement. As seen in Figure 5.17, the maximum temperature reached during the cutting process is 50-60 °C above the room temperature. A calculation done below using the Arrhenius part of HAS model equation and its constants (Q and k_b), discussed in Chapter 4, shows that the Arrhenius term is extremely low at a processing temperature of 350 K.

$$\exp(-Q/k_bT) = \exp(-2.2/(8.6 \times 10^{-5} \times 350)) \approx 10^{-34}$$

Furthermore, due to the presence of initial dislocation density of 10^6 cm^{-2} already in

the workpiece, there is a large back stress against the movement of dislocations. Under these circumstances, inelastic deformation due to the HAS constitutive behaviour is unlikely. This, therefore, suggests that the processing conditions *during sawing* should not have any effect on the warpage in wafers. However, with a different supplied constitute behaviour of mc-Si, that might not be the case.

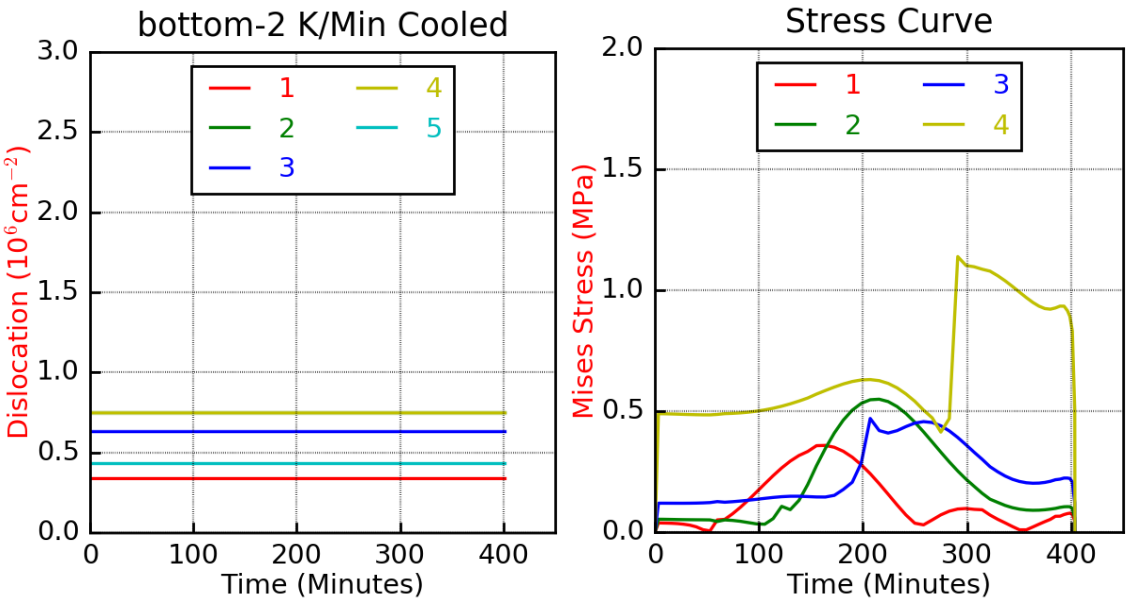

Figure 5.19: Plot of dislocation density and mises stress with time from the temperature coupled stress simulation of wire sawing of 2 K/min cooled ingot.

Under the absence of any inelastic behaviour, the warpage is expected to occur only due to initial residual stress present in the work piece and the location of cut. With this assumption, the wire sawing stress model was simplified by ignoring the change in the temperature during the cutting process. This assumption is valid since thermal strain (which is the cause of warpage) developed during the sawing process should not have in-plane (xz plane) gradient. This is so because of the assumption made in the wire sawing thermal model that the temperature does not vary along the axis of the work-piece.

The final warpage in the wafers predicted by the simulation is summarised as contour plots in Figure 5.20-5.22. These contours show the change in the 'Y' coordinates (with respect to the initial position) for all the points on the wafers cut from

the top, middle and bottom section of 2, 5 and 8 K/min cooled ingots. Overall, all the points on the surface have a warpage of <1 μm. This is considerably less than the expected warpage of 10-15 μm [2]. A summary of the warpage in the mid plane along the movement of the wire is given in Figure 5.23. As expected, the warpage is lowest in wafer cut from the 2 K/min cooled ingot since it has the least amount of residual stress. Furthermore, for all the ingots, the warpage is at a minimum in the middle section and maximum in the top section. This uniformity in the variation in the warpage for all ingots can be explained based on the fact that, as discussed in the casting simulation results, the variation in the residual stress after solidification is the least in the middle/bulk of the ingot. The warpage should be governed by in-plane stress gradient. Since this gradient is lowest in the middle, the warpage is lowest in the middle. These warpage plots also show the presence of surface roughness indicated by the unevenness in the curves.

The variation in the in-plane stress (σ_x) with location along the mid plane of the wafer before and end of the cutting process is plotted in Figure 5.24. This figure summarises the stress relaxation that occurs in form of bending of wafer. As seen, the stress levels decrease significantly due to the re-equilibrium of the forces post removal of layers. The dependence of the warpage with stress should be an analytical function of the in-plane stress components σ_x, σ_z and the shear stress σ_{xz}, σ_{xy} and σ_{zy}. This quantitative comparison is not done here and is left for future work.

The movement of the points on the wafer surface in the 'Y' direction with time is shown in Figure 5.25-5.27. It can be seen that the movement is not unidirectional. This may be due to the changing nature of stress gradients with the location in the work-piece. The time-wise deflection of the points are highest in case 8 K/min cooled due to a higher stress gradient level. These deflections are, however, not very large enough for the adjacent wafers to collide with each other during the sawing process as the gap between adjacent wafers is 500 μm.

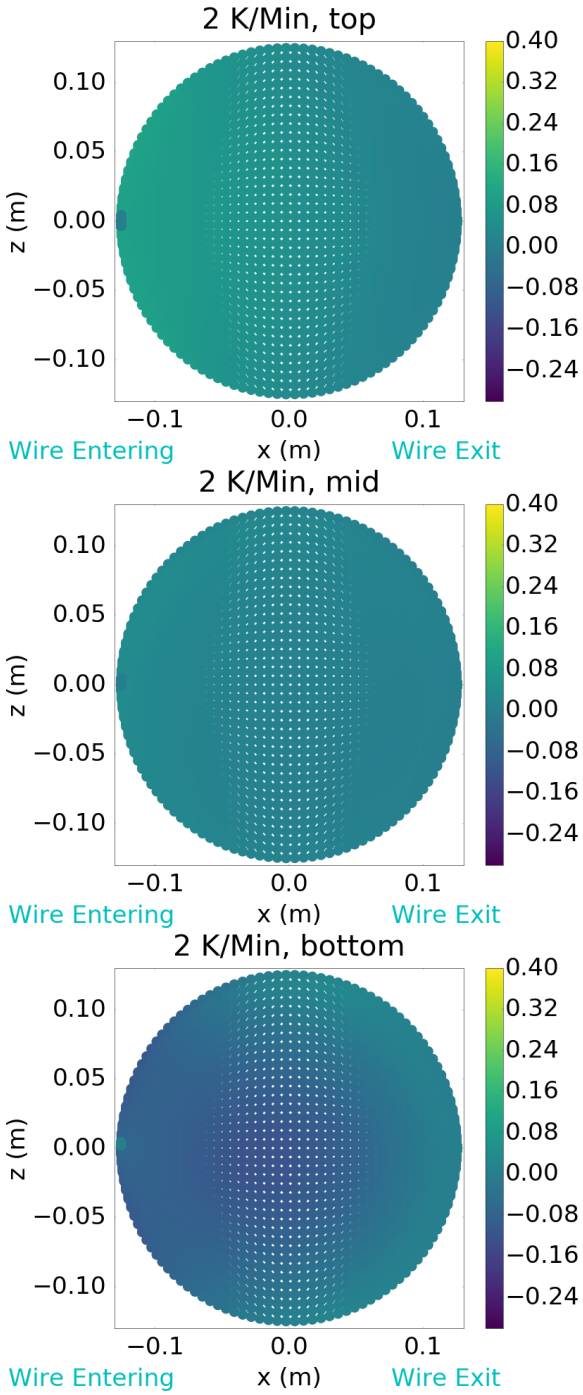

Figure 5.20: Contour plot to show the final warpage (given by the displacement in 'Y' direction from the initial position) in the wafers cut from the top, mid and bottom of 2 K/min cooled ingots. The wire movement is from left to right, implying that the strain energy is higher in the later stages of cutting.

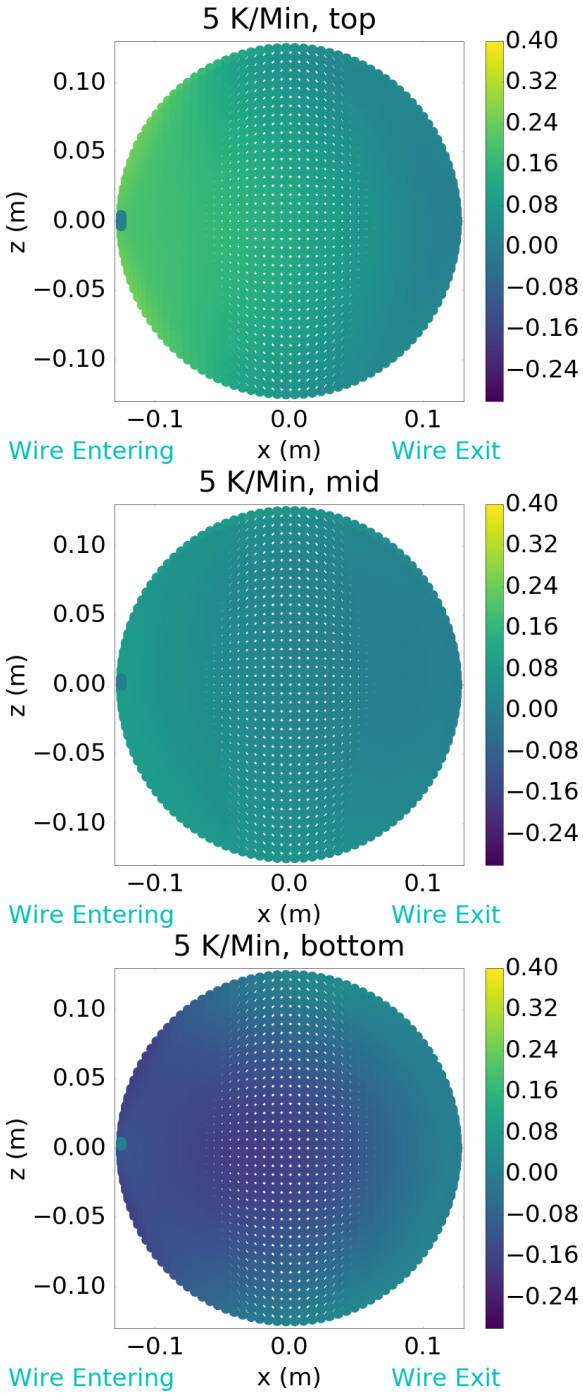

Figure 5.21: Contour plot to show the final warpage (given by the displacement in 'Y' direction from the initial position) in the wafers cut from the top, mid and bottom of 5 K/min cooled ingots. The wire movement is from left to right, implying that the strain energy is higher in the later stages of cutting.

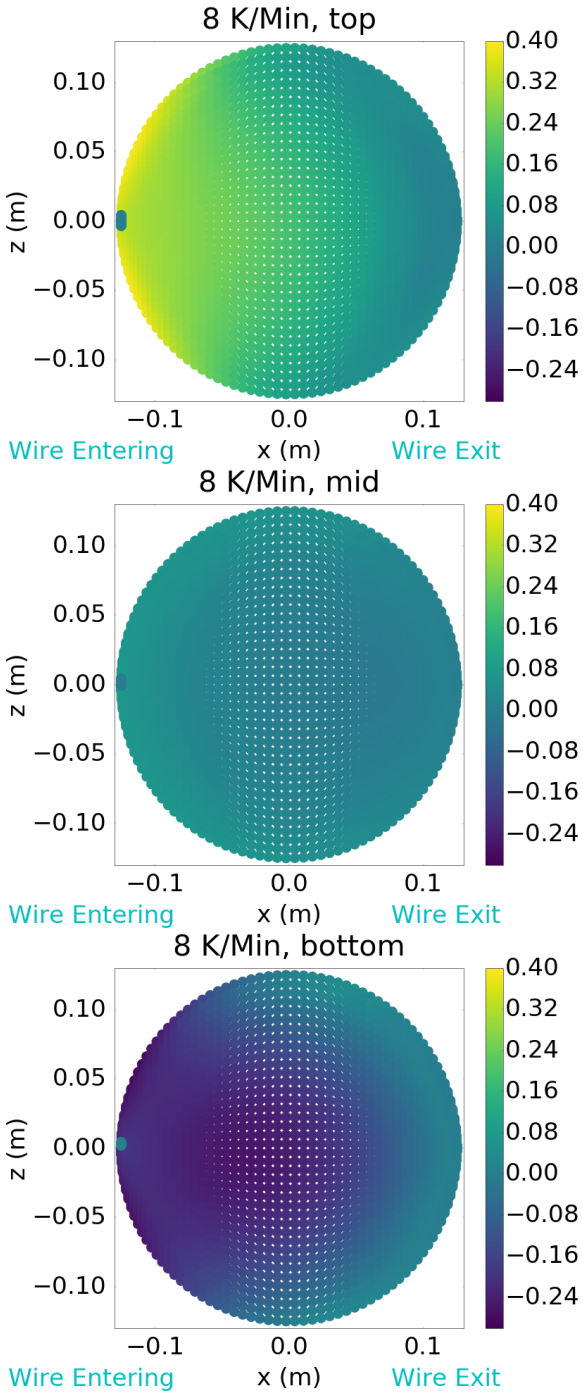

Figure 5.22: Contour plot to show the final warpage (given by the displacement in 'Y' direction from the initial position) in the wafers cut from the top, mid and bottom of 8 K/min cooled ingots. The wire movement is from left to right, implying that the strain energy is higher in the later stages of cutting.

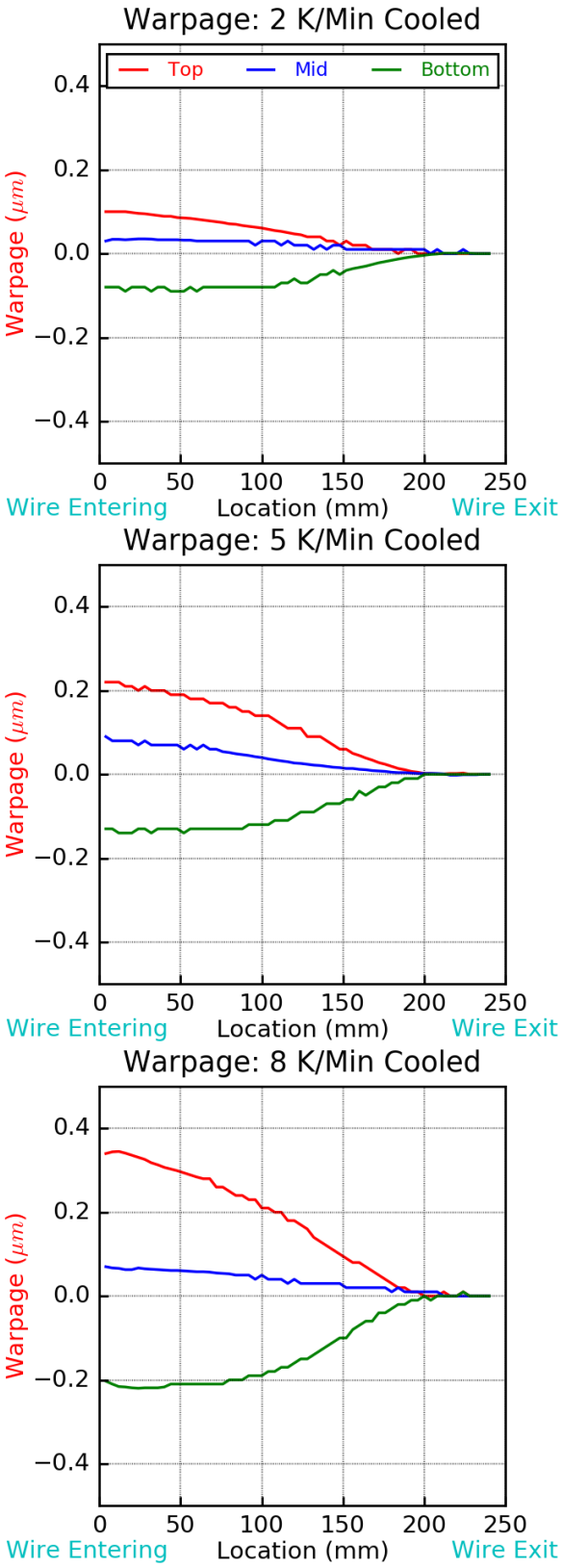

Figure 5.23: Comparison of the final warpage (given by the displacement in 'Y' direction from the initial position) in the wafers cut from the top, mid and bottom of 2, 5 and 8 K/min cooled ingots.

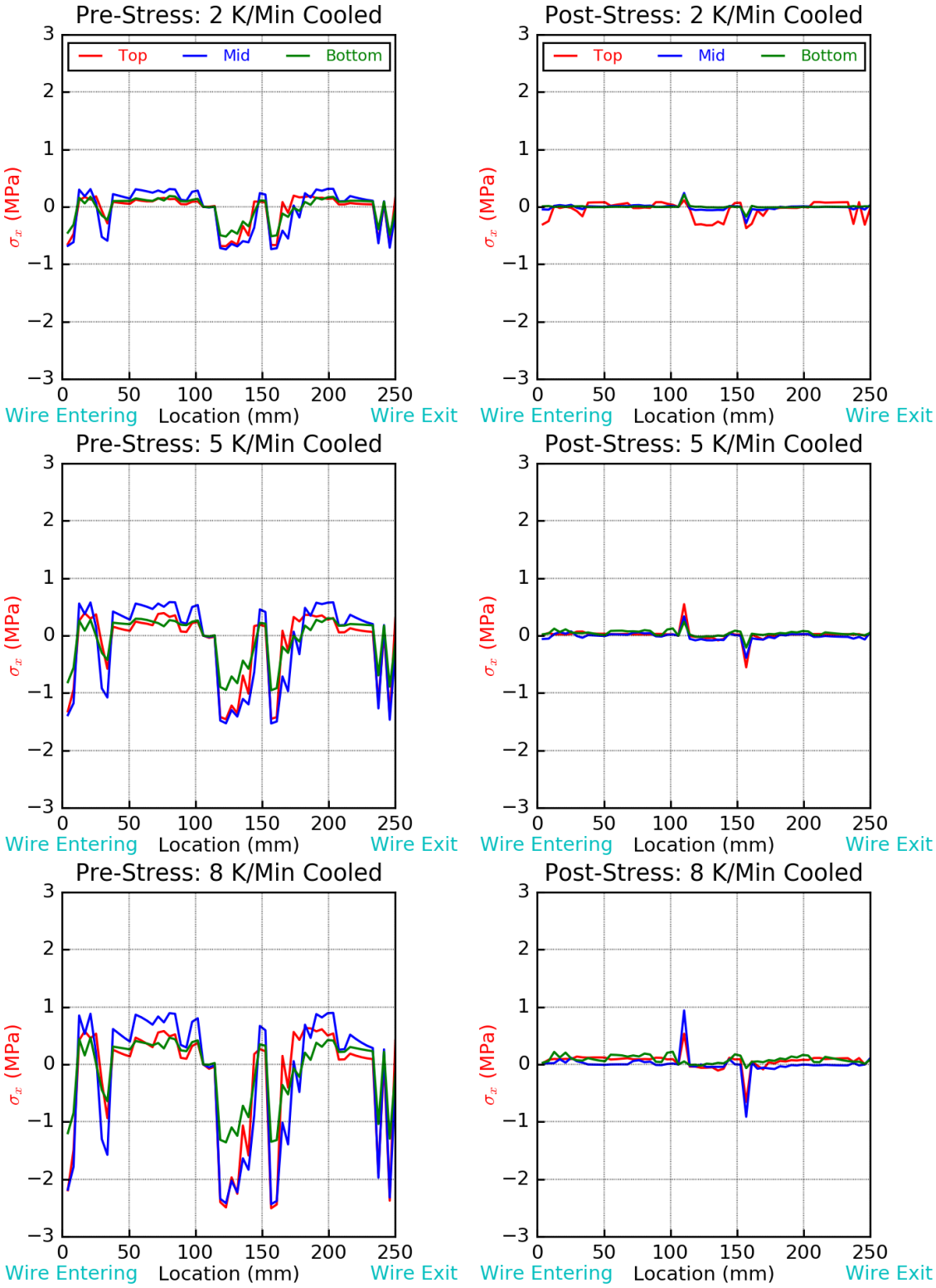

Figure 5.24: Comparison of the initial and the final σ_x in the wafers cut from the top, mid and bottom of 2, 5 and 8 K/min cooled ingots.

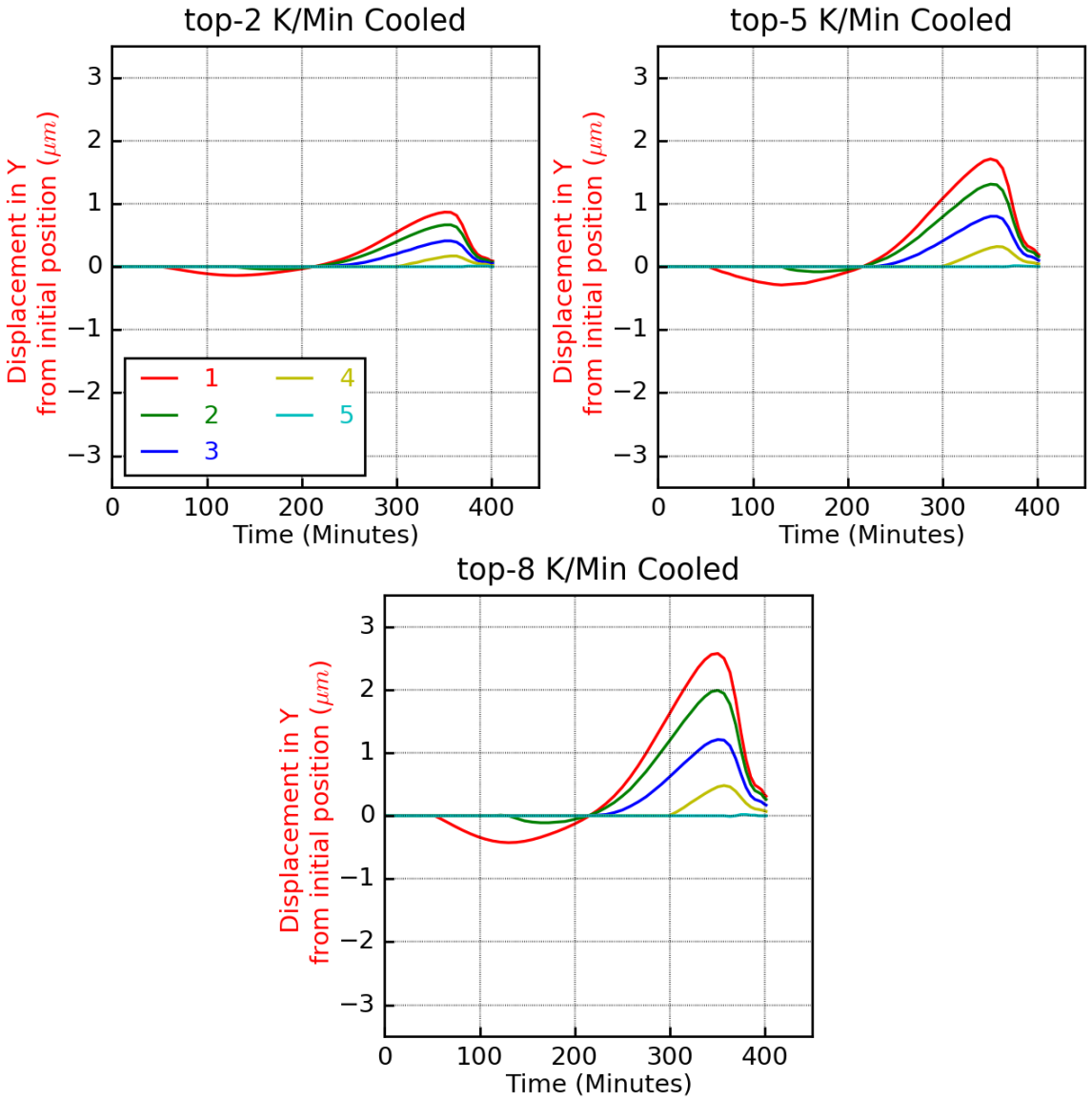

Figure 5.25: Comparison of the deflection of points on the wafers (at Z=0) in the 'Y' direction and the dislocation density with time in the wafers cut from the top of 2, 5 and 8 K/min cooled ingots.

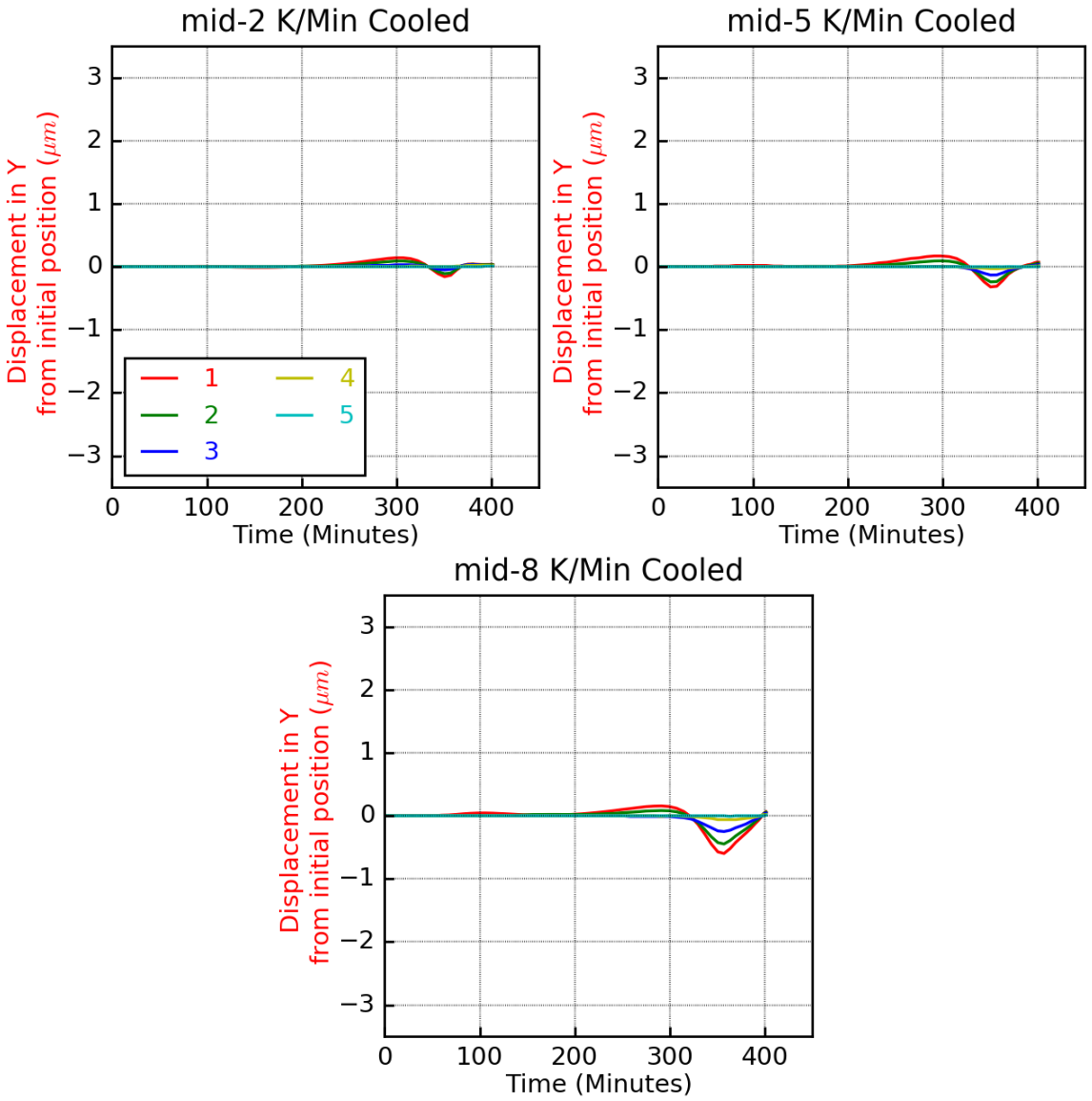

Figure 5.26: Comparison of the deflection of points on the wafers (at Z=0) in the 'Y' direction and the dislocation density with time in the wafers cut from the middle of 2, 5 and 8 K/min cooled ingots.

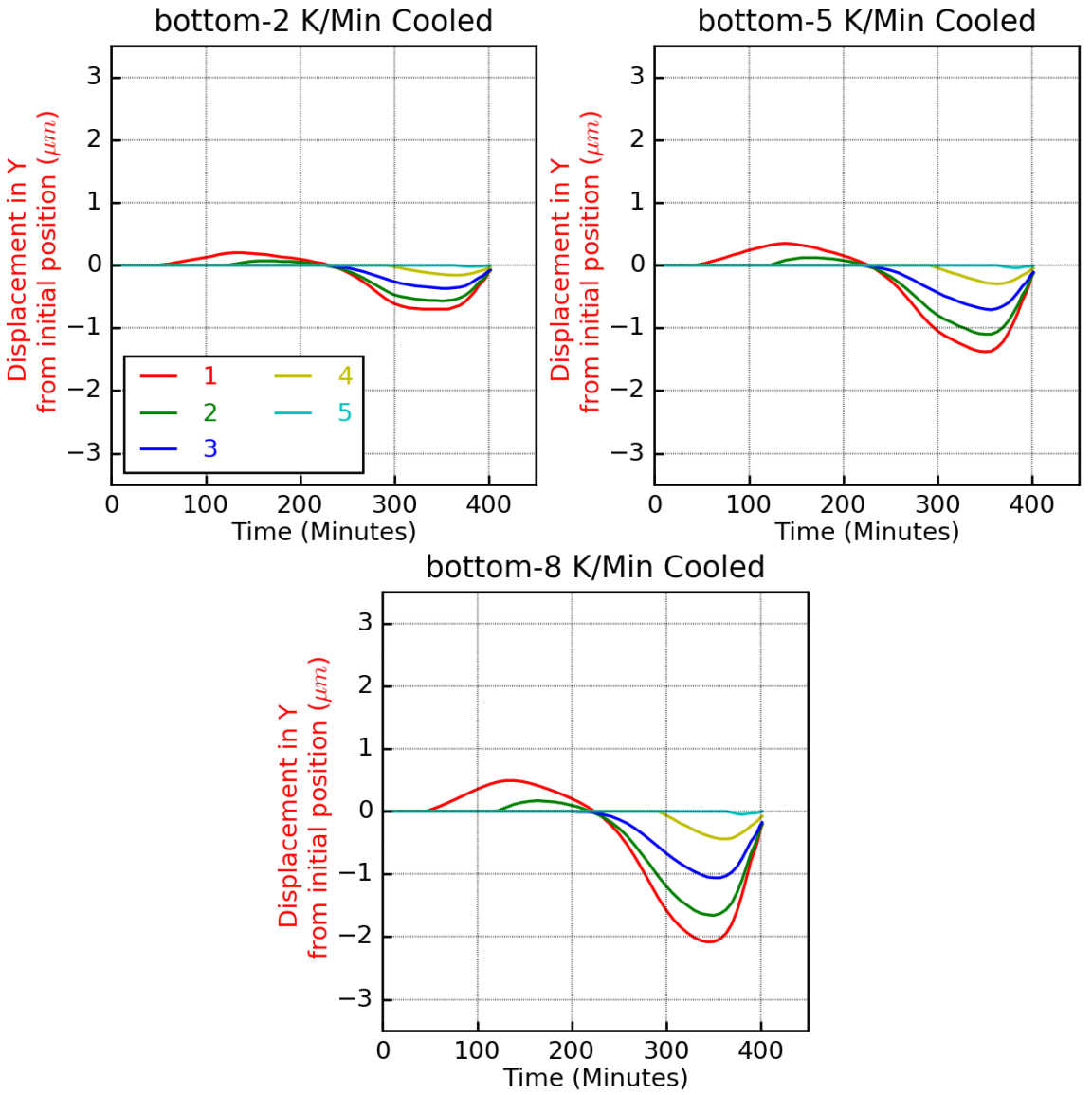

Figure 5.27: Comparison of the deflection of points on the wafers (at Z=0) in the 'Y' direction and the dislocation density with time in the wafers cut from the bottom of 2, 5 and 8 K/min cooled ingots.

High levels of stress release during any machining process and this may lead to material/work-piece breakage. Drezet *et al* [10] have developed a finite element model to simulate the sawing process of aluminium to characterise the effects of initial stress present in the work piece on fracture during sawing. Similar to the current work, they have simulated the sawing process as successive removal of layers in Abaqus through model change. They have used the magnitude of strain energy released at each step of element removal as a parameter to quantify the chances of failure. The same strategy was followed in this study, and strain energy was plotted with time to understand

its variation with time. This is shown in Figure 5.28, which depicts the variations in strain energy per area on locations on the mid plane of 8 K/min cooled ingot along the direction of cutting. The drop in the curve indicates the material removal and the subsequent energy release due to the balance of force fields after element removal. The energy release is predicted to be maximum for the middle wafer, indicating a higher failure chances. This is interesting, since the middle section has the least warpage. It means that the wafer removed from the middle of the work piece is better in terms of the surface quality but is at a higher risk of being damaged during the sawing process.

5.6 Results Summary

This chapter presents the results of the thermo-mechanical simulations performed to characterise the mc-Si solidification and wire sawing processes. The results of the simulation quantitatively predict the warpage and dislocation density in the wafers cut from directionally solidified ingots and its dependence on the cooling rate during the solidification of the said ingots. The observed wafer warpage in industrial settings is around 10-15 μm, as discussed in Chapter 1. The current model was able to predict a maximum warpage of 1 μm. The overall prediction was currently not validated against any actual data and is left as a future work.

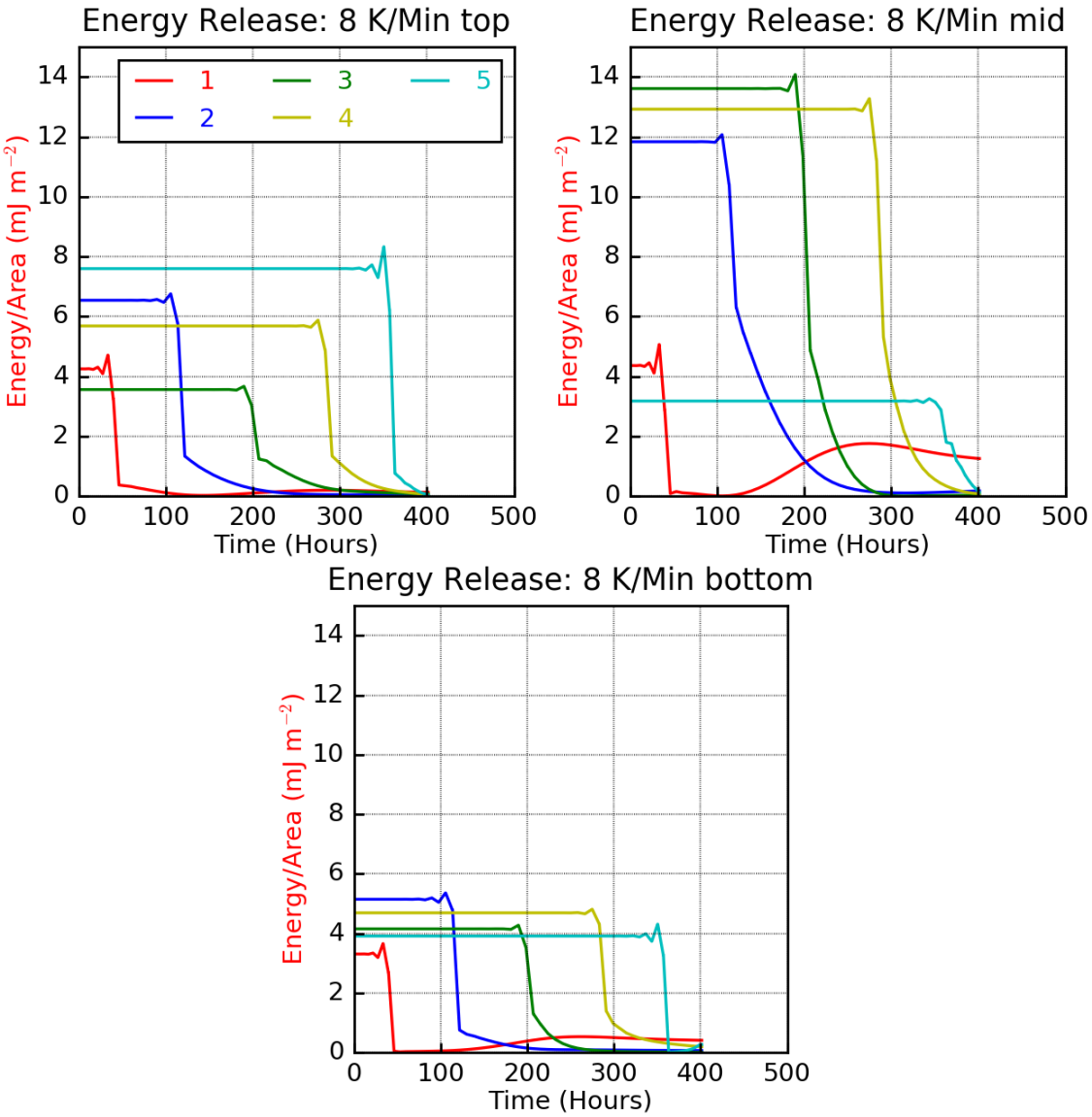

Figure 5.28: Plot to show the variation of strain energy (kJ m^{-2}) with time along the direction of cutting at locations on the mid plane of the wafer cut from 8K/min cooled ingot. The wire movement is from point 1 to 5. Mid section has the highest energy release.

Chapter 6

Summary and Conclusions

6.1 Model development

A finite element model was developed to simulate the stress/strain, dislocation density and warpage in wafers produced via wire sawing of directionally solidified mc-Si ingots. Separate thermo-mechanical models were developed for both directional solidification and wire sawing processes. Both of these two models were transient in nature and were sequentially coupled. These stress models used the HAS model [14] as the input constitutive behaviour of mc-Si. The HAS model connects the growth and multiplication of dislocations in a crystal with the applied stress fields. This growth and multiplication of dislocations relieves stress and leads to inelastic deformations. The sources of stress during casting and wire sawing is the strain developed due to thermal gradient. Thermal gradients arise during these processes due to non-uniform cooling/heating conditions or geometrical factors. The heating/cooling conditions and the geometry, therefore, were the design parameters in the thermal simulations. Temperature data from these thermal simulations were then used as a temperature boundary condition in simulating the thermal strains and the dislocation-creep.

6.2 Mc-Si casting simulation

The casting simulation was started with the thermal model. Cooling of the ingot domain for this simulation was done from 1500 °C to 25 °C and was simulated by reducing the bottom surface nodes temperature at 2, 5 and 8 K/min. These cooling conditions simulated the dislocation growth at slow, medium, and fasting cooling in

mc-Si ingots during directional solidification. The cooling conditions were supplied as Dirichlet boundary conditions. It was observed that with the increase in cooling rate, the overall dislocation density in the ingot increased. This was expected and in accordance with the literature [12]. The spatial variation in dislocation density in the ingot increased with the increase in cooling rate. It was also found that the dislocation growth occurred at high stress and high temperature only. The rate of cooling influenced the inelastic strains and dislocation density only in the early stages of cooling. This could mean that cooling rate can be increased in the later stages to reduce the overall solidification/casting time without much increase in the dislocation density.

6.3 Wire sawing simulation

The thermal model developed using the analytical model of wire sawing [4, 31] provided temperature variations during the wire sawing process. The stress model developed using this thermal model predicted no inelastic deformation in the wafers during sawing. Based on this model, it was also found that the initial residual stress in the work piece had an effect on the warpage in the wafers. The wafer cut from top, middle and bottom of the work piece had different amount of warpage. The model also provided an insight of the strain energy released during cutting. Based on this energy release, it was said that the risk of fracture is higher in the middle section of the work piece during the sawing process.

6.4 Future work

This new tool is a significant advancement, coupling simulations of casting and wire sawing in order to predict dislocation density and warpage in mc-Si wafers. However, there are several assumptions and simplifications used in this work that could be improved in order to match industrial processing. The casting model could be improved

by providing the actual cooling rate and the surface cooling coefficient from an industrial setting. This would help in building a better model by validating the predicted dislocation density against the observed etch pitch density in the ingot. The thermal model of wire sawing could also be improved. Heat transfer during wire sawing is quite complex due to the movement of slurry/wire and the changing geometry with time. Experimental data could help train the numerical model better in terms of predicting the temperature variations and gradients. In short, the model developed in this study could be improved by validating them against real world data and by implementing even more sophisticated mathematical model to overcome some of the simplifications and assumptions made.

Bibliography

[1] H Alexander and P Haasen. Dislocations and plastic flow in the diamond structure. *Solid state physics*, 22:27–158, 1969.

[2] Yasuharu Ariga. Wire saw and cutting method, November 25 2003. US Patent 6,652,356.

[3] M Bhagavat, V Prasad, and I Kao. Elasto-hydrodynamic interaction in the free abrasive wafer slicing using a wiresaw: modeling and finite element analysis. *Journal of Tribology*, 122(2):394–404, 2000.

[4] Sumeet Bhagavat and Imin Kao. A finite element analysis of temperature variation in silicon wafers during wiresaw slicing. *International Journal of Machine Tools and Manufacture*, 48(1):95–106, 2008.

[5] A Bidiville, K Wasmer, J Michler, PM Nasch, M Van der Meer, and C Ballif. Mechanisms of wafer sawing and impact on wafer properties. *Progress in Photovoltaics: Research and Applications*, 18(8):563–572, 2010.

[6] J Cochard, I Yonenaga, S Gouttebroze, M ochardMHamdi, and ZL Zhang. Constitutive modeling of intrinsic and oxygen-contaminated silicon monocrystals in easy glide. *Journal of applied physics*, 108(10):103524, 2010.

[7] J Cochard, I Yonenaga, M M'Hamdi, and ZL Zhang. A novel constitutive model for semiconductors: The case of silicon. *Journal of the Mechanics and Physics of Solids*, 61(12):2402–2432, 2013.

[8] Gianluca Coletti, Paula CP Bronsveld, Giso Hahn, Wilhelm Warta, Daniel Macdonald, Bruno Ceccaroli, Karsten Wambach, Nam Le Quang, and Juan M Fer-

nandez. Impact of metal contamination in silicon solar cells. *Advanced Functional Materials*, 21(5):879–890, 2011.

[9] JR Davis, Ajeet Rohatgi, Richard H Hopkins, Philip D Blais, P Rai-Choudhury, James R Mccormick, and HC Mollenkopf. Impurities in silicon solar cells. *IEEE Transactions on Electron Devices*, 27(4):677–687, 1980.

[10] J-M Drezet, Olivier Ludwig, C Jacquerod, and Emmanuel Waz. Fracture prediction during sawing of dc cast high strength aluminium alloy rolling slabs. *International Journal of Cast Metals Research*, 20(3):163–170, 2007.

[11] Guoping Du, Nan Chen, and Pietro Rossetto. On-wafer investigation of sic and si 3 n 4 inclusions in multicrystalline si grown by directional solidification. *Solar Energy Materials and Solar Cells*, 92(9):1059–1066, 2008.

[12] D Franke, T Rettelbach, C Häßler, W Koch, and A Müller. Silicon ingot casting: process development by numerical simulations. *Solar energy materials and solar cells*, 72(1):83–92, 2002.

[13] CJ Glassbrenner and Glen A Slack. Thermal conductivity of silicon and germanium from 3 k to the melting point. *Physical Review*, 134(4A):A1058, 1964.

[14] P Haasen. Zur plastischen verformung von germanium und insb. *Zeitschrift für Physik*, 167(4):461–467, 1962.

[15] Robert Hull. *Properties of crystalline silicon*. Number 20 in 1. IET, 1999.

[16] Masato Imai and Koji Sumino. In situ x-ray topographic study of the dislocation mobility in high-purity and impurity-doped silicon crystals. *Philosophical Magazine A*, 47(4):599–621, 1983.

[17] Makoto Inoue, Satoshi Nakano, Hirofumi Harada, Yoshiji Miyamura, Bing Gao, Yoshihiro Kangawa, and Koichi Kakimoto. Numerical analysis of the dislocation density in multicrystalline silicon for solar cells by the vertical bridgman process. *International Journal of Photoenergy*, 2013, 2013.

[18] AA Istratov, T Buonassisi, RJ McDonald, AR Smith, R Schindler, JA Rand, J Pl Kalejs, and ER Weber. Metal content of multicrystalline silicon for solar cells and its impact on minority carrier diffusion length. *Journal of Applied Physics*, 94(10):6552–6559, 2003.

[19] A_S Jordan, R Caruso, and AR Neida. A thermoelastic analysis of dislocation generation in pulled gaas crystals. *Bell System Technical Journal*, 59(4):593–637, 1980.

[20] A Kailer, Yu G Gogotsi, and KG Nickel. Phase transformations of silicon caused by contact loading. *Journal of applied physics*, 81(7):3057–3063, 1997.

[21] JP Kalejs. Modeling contributions in commercialization of silicon ribbon growth from the melt. *Journal of crystal growth*, 230(1):10–21, 2001.

[22] Ken-Ichi Kojima and Koji SUMINO. Strain-rate and temperature dependence of mechanical behaviour in germanium crystals. *Science reports of the Research Institutes, Tohoku University. Ser. A, Physics, chemistry and metallurgy*, 23:211, 1971.

[23] J Li, I Kao, and V Prasad. Modeling stresses of contacts in wire saw slicing of polycrystalline and crystalline ingots: application to silicon wafer production. *Journal of Electronic Packaging*, 120(2):123–128, 1998.

[24] K Liu, XP Li, and SY Liang. The mechanism of ductile chip formation in cutting of brittle materials. *The International Journal of Advanced Manufacturing Technology*, 33(9-10):875–884, 2007.

[25] Holger Lundt, Lothar Huber, and Peter Wiesner. Method for cutting slices from a workpiece, August 10 2004. US Patent 6,773,333.

[26] DM Maijer, T Ikeda, SL Cockcroft, M Maeda, and RB Rogge. Mathematical modeling of residual stress formation in electron beam remelting and refining

of scrap silicon for the production of solar-grade silicon. *Materials Science and Engineering: A*, 390(1):188–201, 2005.

[27] Dimitris Maroudas and Robert A Brown. On the prediction of dislocation formation in semiconductor crystals grown from the melt: analysis of the haasen model for plastic deformation dynamics. *Journal of crystal growth*, 108(1):399–415, 1991.

[28] Ernst A Meese, Harald Laux, Eivind J Øvrelid, et al. Thermo-mechanical analysis of directional crystallisation of multi-crystalline silicon ingots. In *Materials Science Forum*, volume 508, pages 597–602. Trans Tech Publ, 2006.

[29] N Miyazaki. Dislocation density evaluation using dislocation kinetics model. *Journal of crystal growth*, 303(1):302–309, 2007.

[30] Hans Joachim Möller. Basic mechanisms and models of multi-wire sawing. *Advanced Engineering Materials*, 6(7):501–513, 2004.

[31] Hans Joachim Möller, Claudia Funke, Markus Rinio, and Sandra Scholz. Multicrystalline silicon for solar cells. *Thin Solid Films*, 487(1):179–187, 2005.

[32] A Muižnieks, G Raming, A Mühlbauer, J Virbulis, B Hanna, and WV Ammon. Stress-induced dislocation generation in large fz-and cz-silicon single crystalsnumerical model and qualitative considerations. *Journal of crystal growth*, 230(1):305–313, 2001.

[33] S Nakano, XJ Chen, B Gao, and K Kakimoto. Numerical analysis of cooling rate dependence on dislocation density in multicrystalline silicon for solar cells. *Journal of Crystal Growth*, 318(1):280–282, 2011.

[34] Yasumasa Okada and Yozo Tokumaru. Precise determination of lattice parameter and thermal expansion coefficient of silicon between 300 and 1500 k. *Journal of applied physics*, 56(2):314–320, 1984.

[35] AS Okhotin, AS Pushkarski, and VV Gorbachev. Thermophysical properties of semiconductors", moscow," atom" publ, 1972.

[36] JR Patel and AR Chaudhuri. Macroscopic plastic properties of dislocation-free germanium and other semiconductor crystals. i. yield behavior. *Journal of Applied Physics*, 34(9):2788–2799, 1963.

[37] B Ryningen, G Stokkan, M Kivambe, T Ervik, and O Lohne. Growth of dislocation clusters during directional solidification of multicrystalline silicon ingots. *Acta Materialia*, 59(20):7703–7710, 2011.

[38] Wahid Shams-Kolahi, Harry Ruda, and Christina F Souza. Method for purifying metallurgical silicon, December 19 2013. US Patent App. 14/653,580.

[39] Adam Sieminski. International energy outlook. *Energy Information Administration (EIA)*, 2014.

[40] H Siethoff, K Ahlborn, and HG Brion. The effect of solutes on the dynamical recovery of silicon and germanium. *Acta metallurgica et materialia*, 39(6):1133–1140, 1991.

[41] H Siethoff, P Haasen, and HR Hasiguti. Lattice defects in semiconductors. *University of Tokyo, Tokyo*, page 491, 1968.

[42] Hans Siethoff and Hans Georg Brion. The deformation regimes of the yield point of silicon. *Philosophical Magazine A*, 81(1):145–152, 2001.

[43] Koji Sumino. Deformation behavior of silicon. *Metallurgical and Materials Transactions A*, 30(6):1465–1479, 1999.

[44] Isao Takahashi, Noritaka Usami, Kentaro Kutsukake, Gaute Stokkan, Kohei Morishita, and Kazuo Nakajima. Generation mechanism of dislocations during directional solidification of multicrystalline silicon using artificially designed seed. *Journal of Crystal Growth*, 312(7):897–901, 2010.

[45] Kurt Weiser. Theoretical calculation of distribution coefficients of impurities in germanium and silicon, heats of solid solution. *Journal of Physics and Chemistry of Solids*, 7(2):118–126, 1958.

[46] AE Widmer and W Rehwald. Thermoplastic deformation of silicon wafers. *Journal of The Electrochemical Society*, 133(11):2403–2409, 1986.

[47] Hao Wu, Shreyes N Melkote, and Steven Danyluk. Mechanical strength of silicon wafers cut by loose abrasive slurry and fixed abrasive diamond wire sawing. *Advanced Engineering Materials*, 14(5):342–348, 2012.

[48] Buhle S Xakalashe and M Tangstad. Silicon processing: from quartz to crystalline silicon solar cells. *Chem Technol*, pages 32–7, 2012.

[49] Toshiro YAMADA, Moritaka FUKUNAGA, Takeshi ICHIKAWA, Kazuhiro FURUNO, Kunio MAKINO, and Atsushi YOKOYAMA. Prediction of warping in silicon wafer slicing with wire-saw machine. *Theoretical and Applied Mechanics Japan*, 51:251–258, 2002.

[50] Ichiro Yonenaga and K Sumino. Dislocation dynamics in the plastic deformation of silicon crystals i. experiments. *Physica status solidi (a)*, 50(2):685–693, 1978.

[51] Hongxu Zhao, Ran Jin, Su Wu, and Jianjun Shi. Pde-constrained gaussian process model on material removal rate of wire saw slicing process. *Journal of Manufacturing Science and Engineering*, 133(2):021012, 2011.